Optimisation of functional properties in lead-free BiFeO3–BaTiO3 ceramics through La3+ substitution strategy

DOI:
10.1039/C7TA09497C

Document Version
Accepted author manuscript

Journal of Materials Chemistry A

Accepted Manuscript

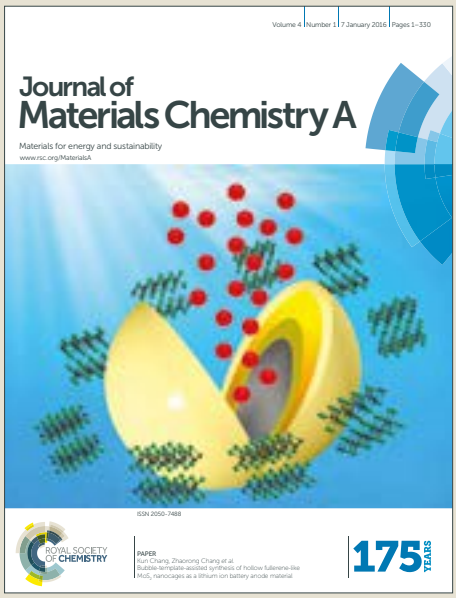

ROYAL SOCIETY OF CHEMISTRY

rsc.li/materials-a

View Article Online
DOI: 10.1039/C7TA09497C

Optimisation of functional properties in lead-free $BiFeO_3$-$BaTiO_3$ ceramics through La^{3+} substitution strategy

Ilkan Calisir,[1] Abdulkarim. A. Amirov,[2,3] Annette K. Kleppe[4] and David A. Hall[1*]

[1]School of Materials, University of Manchester, M13 9PL, Manchester, UK

[2]Center for Functionalized Magnetic Materials (FunMagMa) & Institute of Physics Mathematics and Informational Technologies Immanuel Kant Baltic Federal University, Kaliningrad, Russia

[3]Amirkhanov Institute of Physics Daghestan Scientific Center, Russian Academy of Sciences Makhachkala, Russia

[4]Diamond Light Source Ltd., Harwell Science and Innovation Campus, OX11 0DE, Didcot, UK

[*]Corresponding Author: david.a.hall@manchester.ac.uk

View Article Online
DOI: 10.1039/C7TA09497C

ABSTRACT

The paper is concerned with the structure and functional properties of bismuth ferrite-barium titanate, $0.75BiFeO_3$-$0.25BaTiO_3$, solid solutions. Such materials are attracting attention due to their potential applications in high temperature piezoelectric transducers for use in demanding environments in process monitoring, for example. The article focuses on the mechanism of incorporation of the minor dopant lanthanum oxide, either in the form of isovalent or donor-type substitution. It is shown that the development of chemical heterogeneity in the form of core-shell grain microstructures, linked to donor-type substitution, plays a key role in controlling the functional behaviour. The use of an air-quenching procedure results in dramatic improvements in the ferroelectric properties, accompanied by a transformation of the shell regions from a pseudo-cubic, *Pm-3m*, to rhombohedral, *R3c*, structure. These observations are interpreted in terms of a novel mechanism involving nanoscale phase separation in the 'shell' regions during slow cooling, which impedes the development of ferroelectric ordering and leads to the formation of a nano-polar relaxor ferroelectric state. The work highlights the importance of immiscibility in bismuth-based ferroelectric perovskite solid solutions and illustrates how their ferroelectric, piezoelectric, dielectric energy storage, ferromagnetic and magneto-electric properties can be tuned by consideration of the substitution mechanism and control of thermal processing parameters.

View Article Online
DOI: 10.1039/C7TA09497C

1. INTRODUCTION

In recent decades, there has been intensive research on lead-free electroceramics, with the aim of identifying suitable replacement materials for lead-based ferroelectrics such as lead zirconate titanate (PZT), for example.[1–3] In parallel, multiferroic $BiFeO_3$ has been investigated to provide multifunctionality in current and/or future device applications.[4–6] Increased environmental concerns regarding the usage of 'toxic' lead (Pb) in electronic components have led to EU and worldwide legislation to reduce the use of hazardous substances such as Pb-based oxides in all sectors.[3] Thus, a number of lead-free ferroelectric ceramics to replace PZT have been proposed and developed, including mostly perovskite-structured compounds such as $BaTiO_3$ (BT), $K_{0.5}Na_{0.5}NbO_3$ (KNN), $Bi_{0.5}Na_{0.5}TiO_3$ (BNT) and their modified solid solution systems, including combinations with other perovskites.[3]

KNN-based solid solutions are generally regarded as the leading candidate to replace PZT for piezoelectric applications. However, a revelatory report[7] in 2016 demonstrated that the life cycle stages of KNN, in comparison with PZT, raised serious concerns due to environmental destruction and energy consumption during the mining of Nb_2O_5 which is one of the main constituent oxides in KNN. Thus, the generic term 'lead-free' referring to environmental concerns in the literature (in most cases) may be supplemented by terms such as 'niobium-free' or 'niobium-reduced', in spite of its nontoxicity. In the light of these findings, if the current situation in the mining of niobium oxide does not show any further reformation, it is possible that the focus on finding replacements for lead-based materials may shift to Bi-based titanate solid solutions in perovskites including $(Bi_{0.5}A_{0.5})TiO_3$, A=Na, K and $Bi(B)O_3$, $(Zn_{0.5}Ti_{0.5})$, $(Mg_{0.5}Ti_{0.5})$ or ferrites such as $BiFeO_3$-based ceramics.[8–10]

Among the Bi-based ferroelectric ceramics, $BiFeO_3$ (BF) is renowned as a special compound due to its multiferroic nature at room temperature.[4] Perovskite-structured rhombohedral, *R3c*, $BiFeO_3$ undergoes an antiferromagnetic-paramagnetic phase transition, at T_{Neel}≈370°C and subsequently its ferroelectric nature transforms into paraelectric at T_{Curie} ≈825°C,[4] which is one of the highest amongst perovskite oxides. The intrinsic nature of the large spontaneous polarization, P_s, in single crystal $BiFeO_3$ was reported as ≈100 μC/cm^2 along the pseudocubic $[111]_{pc}$ direction, which is in agreement in ab-inito calculations.[4] On the other hand, a remanent polarisation, P_r, in the region of 20 μC/cm^2 was reported for polycrystalline ceramics prepared using a mechanochemical synthesis method.[6]

Nevertheless, pure $BiFeO_3$ ceramics are not generally considered as promising 'lead-free' ferroelectric/piezoelectric candidates due to several factors including high leakage current, difficulties in poling due to the high coercive field and low piezoelectric coefficients. Processing issues such as the volatility of bismuth oxide at high temperatures, frequent secondary phase formation, structural and thermodynamic instability are also important factors that limit its potential usage in various advanced devices.[4–6,11,12]

On the other hand, in order to reveal its potential multifunctional properties, research studies addressing these issues have recently peaked and the obstacles have been overcome using various processing methods[6,13–16] and/or 'site engineering' by means of partial substitutions

View Article Online
DOI: 10.1039/C7TA09497C

of A– and B– site ions in the perovskite structure of $BiFeO_3$.[17–25] In addition, solid solution formation with other ABO_3-type perovskite ceramics[8,26] has revealed intriguing functional properties in the form of binary,[9,27,28] ternary,[9,29,30] or even quaternary compounds.[31]

Particular attention can be drawn to the formation of $BiFeO_3$–$BaTiO_3$ (BF–BT) solid solutions, which have been intensively studied as promising candidates for high temperature applications,[9,27,32] surpassing the temperature capability of typical lead-based ferroelectrics that possess lower T_C values. Systematic structural studies in the binary xBF–BT system[8,32,33] showed that the major rhombohedral phase, *R3c*, in $BiFeO_3$ gradually transforms into a pseudocubic phase, starting from $x \leq 0.70$ and the occurrence of a *Pm-3m* cubic phase over a wide compositional range gradually disappears above $x \approx 0.10$, resulting in the appearance of tetragonal structure, *P4mm*, which is the characteristic crystal structure of $BaTiO_3$ at room temperature. Regarding the morphotropic phase boundary (MPB), which is often considered as a crucial feature for enhancement of piezoelectric activity, the most active region has been reported[34] to lie in the range $0.67 \leq x \leq 0.70$, where a mixture of pseudocubic and rhombohedral phases is present. This contrasts with the more traditional MPB between rhombohedral and tetragonal phases in PZT and $BiFeO_3$–$PbTiO_3$, for example.[35]

Developments in the processing of BF–BT ceramics have led to enhanced chemical and structural stability in the synthesis of single phase materials and have successfully inhibited the formation of common secondary phases such as $Bi_2Fe_4O_9$, $Bi_{25}FeO_{39}$, and $Bi_{36}Fe_2O_{57}$.[12,36] Furthermore, weak ferromagnetism was reported due to suppression of the spin cycloid structure of $BiFeO_3$ through partial Ba^{2+} and Ti^{4+} substitutions.[33] However, the intrinsic ferroelectric character of $BiFeO_3$ in bulk BF–BT ceramics, in the form of saturated polarisation-electric field (P-E) hysteresis loops, has rarely been reported without any further modification,[27] due to the presence of a relatively high leakage current. Therefore, many researchers have employed additional modifiers, such as MnO_2, in order to increase its insulation behaviour,[27,37,38] although the incorporation route could play a key role in chemical homogeneity as discussed in our previous investigation.[39]

There are few studies focused on the influence of rare-earth ions in BF–BT.[40,41] However, a number of publications have attempted to reveal the effects of substituting rare-earth ions for Bi^{3+} in single-phase $BiFeO_3$, and for Ba^{2+} in single-phase $BaTiO_3$. In the former case, trivalent La^{3+} is considered particularly interesting amongst the rare-earth ions since its ionic radius is similar to that of Bi^{3+}. It was reported that partial substitution of La^{3+} for Bi^{3+} in $BiFeO_3$ can be beneficial to stabilise the crystal structure due to increasing ionic bond strength,[42] to suppress oxygen vacancies and secondary phases mainly caused by volatilisation of bismuth oxide, as well as increasing the magnetocrystalline anisotropy making the spin cycloid energetically unfavourable.[22] Structural studies[22,23] are in general agreement that La^{3+} contents up to ≈12.5 mol% do not change the *R3c* rhombohedral symmetry of $BiFeO_3$, while further additions cause significant structural phase transformations. Reports sometimes diverge at that point, but most observed a transition from rhombohedral, *R3c*, to orthorhombic, *Pnma*, symmetry. Defining the exact phase transition points and crystal symmetries is still open to debate.[22,23]

View Article Online
DOI: 10.1039/C7TA09497C

For the case of La^{3+} doping in $BaTiO_3$, studies[43] have shown that La^{3+} ions preferentially substitute for Ba^{2+} on the A-site, despite the smaller ionic radius. Therefore, this type of incorporation requires charge compensation through creation of negatively charged defects such as cation vacancies, anion interstitials, electrons, or acceptor impurities.[44] It is well known that at low La^{3+} dopant concentrations (≈0.5 mol%), donor-doped $BaTiO_3$ exhibits semiconductive behaviour due to electronic compensation, while further La^{3+} additions result in insulating behaviour due to ionic compensation by cation vacancies. It has been suggested that the increase in resistivity could be due to reoxidation of ceramics during cooling[45] rather than switching between electronic and ionic charge compensation.[44,46] It is also reported that with increasing La^{3+} content, the formation of Ti vacancies becomes more favourable, according to the formula $Ba_{1-x}La_xTi_{1-x/4}(V_{Ti}^{////})_{x/4}O_3$.[43,44,46] The solid solubility limit has been found to occur at $x \geq 0.25$ in $BaTiO_3$ ceramics, with further additions leading to the formation of secondary phases formed by expelled oxides.[44,46]

In recent years, it has been found that significant enhancements in the functional properties of BF-BT ceramics can be achieved either by compositional trials using certain dopants[27,37,47] or by thermal quenching treatments.[48–50] However, no single report has addressed the underlying mechanisms responsible for these improvements or, sometimes, apparent degradation. Therefore, we aim to investigate the origins of the reported improvements in functional properties and identify how the properties can be optimised. We also questioned why some previous studies reported that donor doped BF-BT ceramics display significant reductions in remanent polarisation, which makes them promising candidates for energy storage dielectrics,[51] and/or high precision actuators due to reduced hysteresis.[52]

The rationale of the present study was to employ both isovalent and aliovalent substitutions of La^{3+} for Bi^{3+} and Ba^{2+} respectively, in the solid solution $0.75BiFeO_3$-$0.25BaTiO_3$ (75BFBT). This solid solution system was selected due to its proximity to the MPB and the existence of a major rhombohedral phase, which enables any possible structural distortions induced by La^{3+} substitution to be identified. It was found that the major determining factor for high performance in BF-BT ceramics is the state of chemical homogeneity; isovalent doping promotes the solubility and leads to a relatively homogeneous microstructure while donor doping reduces the solubility and causes chemical heterogeneity. The formation of core-shell microstructures in the donor-doped BF-BT ceramics hinders ferroelectric polarisation switching. However, it is shown that thermal quenching has a profound impact on the structure of the shell regions, leading to significant changes in functional properties.

View Article Online
DOI: 10.1039/C7TA09497C

2. EXPERIMENTAL PROCEDURES

2.1 Ceramic processing

La-substituted ceramics were synthesised based on the chemical formula of $0.75(Bi_{0.99}La_{0.01})FeO_3$-$0.25BaTiO_3$ and $0.75BiFeO_3$-$0.25(Ba_{0.99}La_{0.01})TiO_3$ using conventional solid state reaction method. The ceramics are hereafter named as *LaBi* and *LaBa* corresponding to which substitution mechanism is involved, the former being isovalent and the latter aliovalent (donor) type. The undoped composition, abbreviated as 75BFBT, was also prepared to provide a reference for comparing the effects of the La substitutions. Bi_2O_3 (99%, Alfa Aesar), Fe_2O_3 (99%, Sigma Aldrich), $BaCO_3$ (99%, Alfa Aesar), TiO_2 (99%, Fisher Scientific) and La_2O_3 (99.9% Alfa Aesar) were used as precursor powders. 2 mol% Bi_2O_3 excess was added into all compositions in order to compensate for the loss of this volatile oxide during sintering. Additional compositions were also prepared, containing 3 and 5 mol% La substituted for both Bi and Ba, in order to assess the influence of increasing La concentrations on the structure and functional properties.

The precursor oxides were weighed according to the required stoichiometric ratios, then mixed and milled for 24 h using propan-2-ol and yttria-stabilized zirconia media. The milled powders were dried at 85°C overnight followed by calcination at 850°C for 2 h with heating and cooling rates of 5°C/min. Additional milling was performed again on the calcined powders for 24 h to reduce the particle size down to the sub-micron region. Polyethylene glycol (PEG1500 with an average molar mass of 1500 g mol^{-1}) solution as a lubricant was added into the calcined powders at a concentration of 2 *wt*% in order to improve compaction behaviour. The calcined powders were uniaxially cold-pressed at ≈150 MPa into 8 mm diameter pellets. The pellets were placed on a layer of calcined powder having the same composition and covered with an inverted alumina crucible, in order to create a bismuth-rich atmosphere and also to avoid possible reaction with the supporting alumina plate.[6] The organic additive was burnt-out at a temperature of 600°C for 1 h, following which the ceramics were sintered at a temperature of 1050°C for 2 h in air, using heating and cooling rates of 5°C/min. Additionally, the produced as-sintered *LaBa* composition was annealed at 800°C for 20 min in air, then directly quenched to room temperature, referred to below as *quenched-LaBa*.

The bulk densities of the sintered ceramics were measured by immersion in distilled water using the Archimedes method. Theoretical densities were obtained on the basis of the structural analysis described below, using the unit cell volume determined from full-pattern refinement of the x-ray diffraction patterns and the nominal chemical composition. The relative densities of the sintered ceramics were calculated as the ratio of bulk to theoretical density and found to be in the region of 95 ± 3% for all of the samples prepared during the present study.

View Article Online
DOI: 10.1039/C7TA09497C

2.2 High Resolution Structural Characterisation

High resolution synchrotron x-ray powder diffraction (SXPD) patterns were collected on the I11 powder diffraction beamline at the Diamond Light Source. The crushed powders obtained from sintered samples were placed in a glass capillary tube. Due to high absorption effects associated with bismuth at the synchrotron radiation energy, the beam energy was adjusted to 25 keV and the glass capillaries with 0.3 mm diameter were used. The diffraction profiles were collected at room temperature using the position sensitive detector (PSD). The x-ray photon wavelength, λ, was determined as 0.494216 Å after calibration using a silicon standard powder. The collected data was later refined based on Rietveld analysis using TOPAS *v*5 software.

The ceramic pellets for in-situ high energy x-ray diffraction experiments were prepared by cutting them into dimensions of approximately 0.5 mm (thickness) x 1 mm (width) x 4 mm (length). The experiment was performed on beamline I15 of the Diamond Light Source using high-energy, monochromatic X-rays with a photon energy of 76 keV. The X-ray beam size was 70 μm in diameter. A custom-designed sample holder was used to support the specimen in the beam and provide electrical contacts, the sample being were immersed in silicone oil to avoid arcing during electric field application. The electric field was applied perpendicular to the beam direction using a high voltage amplifier (Matsusada ECA-10). The specimens were subjected to 2 bipolar cycles of an electric field with amplitude 5 kV mm^{-1}, using a step size of 0.5 kV mm^{-1}. 2D diffraction images were recorded using a Perkin-Elmer XRD 1621 flat-panel detector positioned ≈1.1 m from the sample, with a collection time of 10 s. These 2D images were integrated into 24 sectors using *DAWN* software,[53] yielding orientation-dependent 1D XRD patterns. In the present study, attention is focused on grain orientations with scattering vectors either parallel or perpendicular to the electric field direction, denoted as $\Psi=0^{\circ}$ and $\Psi=90^{\circ}$ respectively. The procedures used for application of the electric field and data analysis were similar to those described by Daniel.[54]

2.3 Microstructure and Electrical Characterisation

The sintered ceramic specimens were ground using 800, 1200, 2500 and 4000 grade SiC paper and then fine polishing was carried out with 3, 1 and 0.25 μm diamond paste followed by diluted OP-S silica colloidal suspension. Well-polished samples were chemically etched by immersing into the etchant solution (95% distilled water + 4% HCl + 1% HF) for 5 seconds. Microstructures of etched and non-etched surfaces were examined using a Philips XL30 FEGSEM equipped with EDS.

For electrical measurements, the samples were polished to obtain smooth and parallel surfaces. In order to achieve a sufficiently high electric field for the ferroelectric hysteresis measurements, the thickness of the samples was polished down to ≈0.5 mm. Silver electrode paste (C2000107P3, Gwent Group) was applied on the top and bottom surfaces of LaBi and LaBa ceramics and then fired at 600˚C for 20 min. For the quenched-LaBa, an air-dried silver paint (AGG3691, Agar Scientific, UK) was applied onto both surfaces of the pellets at room temperature in order to avoid changes in the effects induced by quenching.

View Article Online
DOI: 10.1039/C7TA09497C

Ferroelectric P-E hysteresis measurements were carried out using a function generator (HP 33120A) connected to a Chevin Research HV amplifier to generate the desired high voltage. The samples were subjected to 4 cycles of a sinusoidal electric field with a frequency of 2 Hz. The measured current waveform was integrated numerically over time to yield charge and hence the polarisation was calculated as the surface charge density[55]. Low-field dielectric measurements were carried out at fixed frequencies from 1 to 100 kHz over the temperature range from 25 to 670˚C using a HP 4284A Impedance Analyser, Carbolite CWF 12/5 furnace and a desktop computer which was operated by LabView-based program. The measurements were conducted in air using a heating rate of 2˚C/min.

2.4 Ferromagnetic and Magnetoelectric Measurements:

The bulk ceramics for the magnetic measurements were prepared in form of sintered pellets (t ≈0.5 mm). Ferromagnetic M-H hysteresis measurements were carried out using a vibrating sample magnetometer (Lake Shore 7400). The magnetoelectric measurements were carried out using the methodic described by Amirov.[56] Magnetoelectric (ME) signals were measured by a lock-in amplifier (Stanford research system, Model SR830). Prior to ME measurement, the ceramics were poled for 1 hour under electric fields of 0.15 and 3.5 kV mm^{-1}. The Samples were mounted in longitudinal geometry, i.e. ME voltage is parallel to the direction of AC and DC magnetic fields. The ME coefficient, α_{ME} was calculated using the relation:

$$\alpha_{ME} = \frac{dE}{dH} = \frac{1}{b}\frac{dV}{dH} = \frac{1}{b}\frac{V_{AC}}{H_{AC}}$$

where V_{AC} is the magnetically induced AC electric voltage across the sample, H_{AC} is the amplitude of the AC magnetic field, b is the thickness of the sample. The thermal measurements of ME coefficient in the temperature region (100-500 $^{\circ}$C) were performed in a special thermosinsulated clamber, designed for high temperature experiments with a quartz sample holder. A cryogen-free superconducting magnet system with a maximum field of 7 Tesla was used as a source of the magnetic field.

View Article Online
DOI: 10.1039/C7TA09497C

3. RESULTS and DISCUSSION

3.1 Microstructure

For the microstructural examination, chemically etched surfaces of sintered LaBi, LaBa and quenched-LaBa ceramics are presented in Figure 1. Inhomogeneous grain size distributions were observed in both LaBi and LaBa ceramics. However, the range of grain size varied between approximately 4 and 9 μm in LaBi, while that in LaBa compositions was in the range 1 to 5 μm, as can be observed in Fig. 1(a) and (b), respectively. It is evident that large grain size formation could be associated with the isovalent substitution of La^{3+} for Bi^{3+}, which has been reported to enhance the chemical stability of the perovskite structure.[22] However, there was a slight decrease in the average grain size compared with the undoped composition, as given in Figure S1a, which is most likely due to the lower diffusivity of the rare-earth ions. Features associated with ordered ferroelectric domain patterns are also clearly observed throughout the grains in the LaBi ceramics. In contrast, for the case of donor substitution of La^{3+} for Ba^{2+}, the kinetics of grain growth were likely interrupted by factors associated with the creation of charged defects (most likely cation vacancies), which could lead to limited solubility and the possibility of a solute-drag type grain growth retardation mechanism.[24,57–59] It was also observed that retarded grain growth resulted in the formation of chemical heterogeneity in the form of a core-shell type microstructure. In the etched surfaces, the core regions were found to contain distinct ferroelectric domain features, while the shell regions were featureless (Figure 1(b)). Nevertheless, if the LaBa ceramics were quenched after annealing, relatively high domain concentrations were noticed in both core and shell regions, as seen in Figure 1(c).

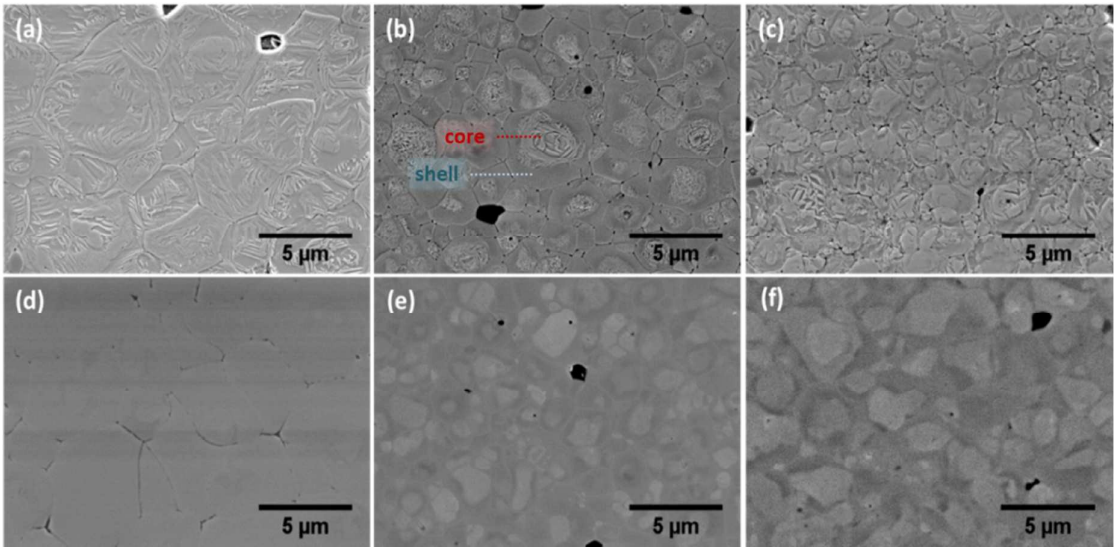

Figure 1. Microstructures of chemically etched sintered surfaces of **a)** LaBi, **b)** LaBa and **c)** quenched-LaBa ceramics. Non-etched polished microstructures of **d)** LaBi, **e)** LaBa and **f)** quenched-LaBa ceramics, which were taken under SEM-backscattered electron (BSE) mode.

View Article Online
DOI: 10.1039/C7TA09497C

Chemically etched sintered surfaces provided invaluable information on the variations in the grain size and domain types, which could be used as strong evidence to correlate the results of structural and electrical characterizations in these ceramics. However, to verify the state of chemical homogeneity, non-etched surfaces of the ceramics were also prepared and examined under the SEM using the backscattered electron (BSE) mode. It was found that there was no clear contrast between core and shell regions in the LaBi ceramics, indicating the chemically homogeneous grain structures (Figure 1(d)). On the other hand, the as-sintered LaBa ceramics showed strong contrast between the core and shell, which correlates well with the features observed in the etched grains, as shown in Figure 1(e). The core regions appear lighter in the BSE images, indicating a concentration of the heavier elements (presumably Bi) in these regions. This type of contrast within the grains was also observed in the non-etched section of the quenched-LaBa ceramic (Figure 1(f)), in contrast to the relatively homogeneous ferroelectric domain distributions in this material (Figure 1(c)). This observation suggests that the quenching process does not significantly affect the micro-scale (core-shell type) chemical heterogeneity in the LaBa ceramic.

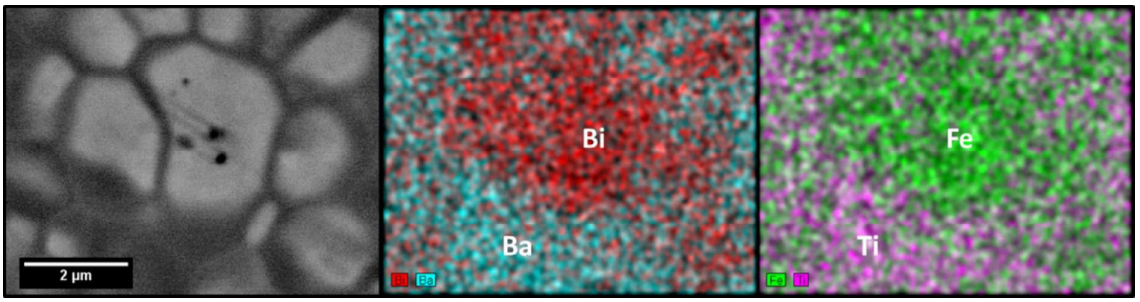

Figure 2. SEM-EDS elemental mapping results of sintered LaBa ceramic exhibiting core-shell grains. Detected elements were also labelled on the regions where were predominantly found.

The occurrence of chemical heterogeneity in the LaBa ceramics was investigated further by means of Energy Dispersive Spectroscopy (EDS). Elemental maps of several grains in the LaBa ceramics are shown in Figure 2. The microsegregation of Bi and Fe elements was clearly detected in the core of grains, corresponding to the lighter regions in the BSE images. In contrast, the signals corresponding to Ba and Ti were mostly evident in the darker shell regions. Due to the small amount of La substitution (1 mol%) in the LaBa ceramics, identification of the La signals from elemental mapping was not feasible. Therefore, we carried out additional EDS investigations on ceramics containing a higher amount of La substitution (3 mol% La^{3+} substituted for Ba^{2+}), yielding the results shown in Figure S2. It was found that the core regions were relatively deficient in La, leading to the conclusion that the shell may show characteristics of La-doped $BaTiO_3$ ceramics.

On increasing the La content to 5 mol%, needle-like secondary phases were formed at the grain boundaries, while the core-shell type micro-segregation became less evident (Figure S3). Due to the small size of these secondary phases, it was challenging to define their chemical compositions using SEM-EDS. Nonetheless, Makovec[44] observed similar types of secondary phases for heavily La-doped $BaTiO_3$ ceramics(≥25 mol% La), which were said to

View Article Online
DOI: 10.1039/C7TA09497C

be associated with the formation of various type of pyrochlore phases due to exceeding the solid solubility limit.

These results demonstrate that 1 mol% donor substitution of La^{3+} for Ba^{2+} in 75BFBT ceramics (LaBa) induced the formation of core-shell type microstructures comprising $BiFeO_3$–rich core and $BaTiO_3$–rich shell regions, with the La^{3+} ions being concentrated in the latter. Increasing levels of substitution led to the disappearance of such features but was also accompanied by the formation of secondary phases, which is indirectly linked to exceeding the solid solubility limit of La^{3+} in in the $BaTiO_3$-enriched shell.

Core-shell type microstructures are a common feature in $BaTiO_3$–based materials[58–60] and can be desirable in order to obtain temperature stable dielectrics.[59,61,62] The core is usually dopant-free, while dopants are mainly segregated in the shell. In the case of the binary solid solution system between $BiFeO_3$ and $BaTiO_3$, differences in reactivity of the constituent oxides are the most likely reason for the occurrence of such features, since it is well established that processing of $BaTiO_3$–based ceramics by solid state reaction methods must be carried out at much higher temperatures than those used for $BiFeO_3$. It was reported that this issue could potentially be overcome by the addition of certain sintering additives/dopants,[27,39,63] increasing the sintering temperature/time[64] or solid solution with other end-members[31] to promote solubility. However, it has been shown that the substitution of 1 mol% La^{3+} for in Ba^{2+} in 75BFBT ceramics leads to the formation of robust chemically heterogeneous microstructures, which are associated with reductions in grain sizes. This could be related to the partial solubility of lanthanum oxide when incorporated in the form of a donor dopant, leading to a solute drag effect on the grain boundaries, as similarly observed in donor Ti^{4+}-substituted $BiFeO_3$.[24]

Relatively homogeneous ferroelectric domain features were noticed throughout the grains regardless of the core and shell regions in the quenched-LaBa ceramics, while the most visible domains were accumulated in the core regions in the as-sintered LaBa ceramics. However the chemical heterogeneity was present in both materials, which could be an indication of possible structural differences in the shell caused by the different cooling procedures. This point is addressed further in the following section.

3.2 Structural Analysis

It has been widely reported that the major phase of the undoped composition (75BFBT) is rhombohedral, with *R3c* space group, which was also verified by our results as shown in Figure S1b. High resolution SXPD measurements were performed to reveal the influence of 1 mol% La substitution for Bi or Ba on the crystal structure of 75BFBT, as well as the effects of air-quenching. The diffraction profiles of LaBi, LaBa and quenched-LaBa ceramics are shown in Figure 3. The diffraction peaks were indexed based on a pseudo-cubic perovskite structure, denoted ‘p’, and the XRD patterns for all compositions confirmed the formation of perovskite solid solutions without any indication of secondary phases. The essential refined crystallographic parameters, together with reliability factors (R-factors), are given in Table 1. It was found that the small amount of La^{3+} substitution for all specimens caused significant structural distortions and the appearance of various fractions of a cubic phase, with space

View Article Online
DOI: 10.1039/C7TA09497C

group *Pm-3m*. Inspection of the $\{111\}_p$ peak profiles reveals the typical peak splitting of the rhombohedral *R3c* phase, indicated by the $(006)_H$ and $(202)_H$ reflections in the hexagonal setting. These peaks are accompanied by the $(111)_C$ cubic *Pm-3m* reflections for all compositions. However, it is evident that the *Pm-3m* phase fractions varied depending on the substitution type and the application of thermal quenching. These effects are a consequence of the changes in chemical homogeneity associated with isovalent (LaBi) and donor (LaBa) substitutions in 75BFBT.

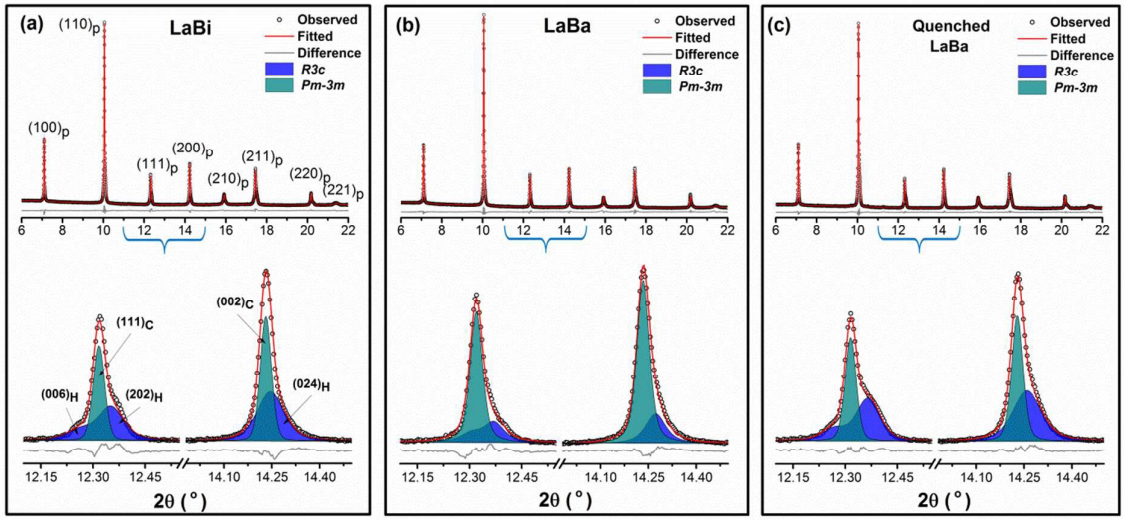

Figure 3. High resolution SXPD patterns and refinements for **a)** LaBi, **b)** LaBa and **c)** quenched-LaBa. The fitted peaks for $\{111\}_p$ and $\{200\}_p$ are highlighted in relation to rhombohedral, *R3c* (doublet of $(006)_H/(202)_H$, and single $(024)_H$ in hexagonal setting), and cubic, *Pm-3m* (single $(111)_C$ and $(002)_C$) phases.

A relatively high *R3c* fraction in LaBi compared to LaBa ceramics could be due to La^{3+} and Bi^{3+} ions sharing similar ionic radii[65] (La^{3+}=1.032 Å and Bi^{3+}=1.03 Å) and the same valence state. Therefore, high structural distortion was not observed or expected in this case. However, structural distortions linked to ferroelectricity are not simply dependent on ionic radii or valence states.[4] The ferroelectric distortion is predominantly contributed by the lone-pair orbital of $Bi^{3+}(6s^2)$ in $BiFeO_3$,[66] but La^{3+} substitution for Bi^{3+} is likely to weaken this lone-pair activity.[4] Therefore, increasing La^{3+} concentration should eventually cause significant structural transformations, as widely reported.[22,23] It should also be noted that the poor perovskite phase stability of $BiFeO_3$ can be improved by La^{3+} substitution since the ionic bond strength can be qualitatively calculated using Pauling's equation given below[67]

$$I_{AB} = 1 - exp[-(\chi_A - \chi_B)^2/4]$$

where I_{AB} is the ionic bond strength with the average electronegativity of anions χ_A and cations χ_B. Based on this equation, the ionic bond strengths of Bi–O and La–O are found to be 0.395 and 0.745, respectively. Therefore, the higher ionic bond strength in La-doped $BiFeO_3$ would make the perovskite phase more stable compared to undoped $BiFeO_3$. A small amount of La was also used effectively in a number of reports to suppress the Bi volatilisation causing serious high leakage current and formation of unwanted phases in pure

View Article Online
DOI: 10.1039/C7TA09497C

$BiFeO_3$ ceramics.[13,68] On the other hand, the observation of a pseudo-cubic phase is commonly reported in rare earth-doped $BiFeO_3$-based solid solution systems[40] where its origin is usually attributed to disruption of ferroelectricity and relaxor ferroelectric character.

In the case of the LaBa ceramics, the highest fraction of *Pm-3m* cubic phase was found for the as-sintered (slow-cooled) material, as illustrated in Figure 3(b). There may be several reasons for this, such as the mismatch of ionic radii[65] (La^{3+}=1.032 Å and Ba^{2+}=1.35 Å) and the aliovalent substitution of La^{3+} for Ba^{2+}, which may have a profound impact on the defect chemistry as well as playing a key role in the diffusion kinetics during heat treatment. Previous reports on the crystal structure of the binary solid solution of BF–BT showed that the cubic phase generally becomes increasingly evident as the $BiFeO_3$ content reduces.[33,69,70] Therefore, any significant deviations in stoichiometry, due to the occurrence of chemical heterogeneity, will favour the formation of the cubic phase in $BiFeO_3$–deficient regions. Microstructural observations of the LaBa ceramics clearly confirmed the formation of chemically heterogeneous grain structures consisting of $BiFeO_3$–rich and –depleted regions in the core and shell, respectively (Figure 2). Hence, this is the most likely reason for the high content of cubic phase, which dominates the SXPD peak profile for this composition.

Table 1. Structural parameters of LaBi, LaBa and quenched-LaBa ceramics obtained from Rietveld refinement. *Goodness of fit (*GoF*) is the value of R_{wp}/R_{exp}.

	LaBi		**LaBa**		**Quenched-LaBa**	
	R3c	Pm-3m	R3c	Pm-3m	R3c	Pm-3m
Phase fractions (%)	40.1(7)	59.9(7)	20.0(4)	80.0(4)	41.3(5)	58.7(5)
Lattice Parameters (Å)						
a	5.6224(4)	3.9902(2)	5.6169(5)	3.9905(3)	5.6170(4)	3.9916(3)
c	13.8829(11)	=*a*	13.8412(18)	=*a*	13.8789(11)	=*a*
Cell Volume ($Å^3$)	380.07(6)	63.533(11)	378.18(9)	63.545(14)	379.22(7)	63.600(12)
R-Factors						
R_{wp} (%)	3.24		3.96		3.22	
R_{exp} (%)	2.02		2.13		1.88	
*GoF**	1.60		1.86		1.71	

Another observation is the presence of significant anisotropic peak broadening for the LaBa ceramics, which could also be a result of the chemical heterogeneity.[71] To overcome this issue during the refinement procedure, the correction proposed by Stephens[72] for materials exhibiting the peak broadening due to 'microstrain' was applied and the fitting was considerably improved. This also implies that compositional fluctuations, taking the form of a core-shell structure in this case, would induce microstrains which may be a key parameter required to correctly refine the structure. The crystal size effect should be also considered as a possible cause of peak broadening. These issues have been recognised in many publications, including those concerned with other $BiFeO_3$-based solid solutions.[28,39,49,73]

In contrast, the diffraction profiles of the thermally quenched-LaBa ceramics were similar to those of the LaBi ceramics. The reappearance of the diffraction peaks associated with the *R3c* phase, as shown in Figure 3(c), is attributed to structural transformations in the shell regions,

View Article Online
DOI: 10.1039/C7TA09497C

induced by the quenching procedure. Evidence for an increased incidence of ferroelectric domain structures, as shown in Figure 1(c), supports this assertion since it is anticipated that the visible domain features should be associated with the ferroelectric *R3c* phase. It should also be mentioned that the apparent cubic phase in BF–BT compositions could actually be rhombohedral or monoclinic on a local scale, as suggested by Singh *et al.*[74]

It is concluded that the process of quenching can transform the featureless pseudo-cubic shell in the LaBa ceramics into rhombohedral ferroelectric domains, as indicated by the increased intensity of the *R3c* reflections in the SXPD profile for the quenched-LaBa ceramics. The underlying cause of this transformation is presently unclear, but it could be associated with nanoscale heterogeneity in the shell regions of the as-sintered (slow-cooled) materials. In turn, this could be a result of immiscibility in the BF–BT system, which would act as a driving force for chemical segregation during cooling and hence would be absent or less effective in the quenched-LaBa ceramics. However, the larger-scale chemical heterogeneity associated with the core-shell microstructure was still maintained regardless of the cooling rate. The occurrence of a significant proportion of cubic phase in the (slow-cooled) LaBi ceramics could also be a result of immiscibility and nanoscale chemical heterogeneity. Further studies involving high resolution TEM would help to test this proposition.

3.3 Dielectric Properties

The variations in the relative dielectric permittivity, ε_r, are employed to evaluate the effects of composition and processing procedures on the ferroelectric phase transformations in these materials. Figure 4 shows the temperature-dependence of the dielectric properties as a function of frequency for LaBi, LaBa and quenched-LaBa ceramics. A single, frequency-independent peak in the ε_r–T plot is usually attributed to the typical ferroelectric to paraelectric transformation, as observed in the case of the LaBi ceramic shown in Figure 4(a). The Curie temperature for this material, which is presumed to be associated with the rhombohedral *R3c* to cubic *Pm-3m* transformation, was found to be approximately 490 °C from these results. Furthermore, the presence of a frequency-dependent shoulder in the temperature range from 300 to 400 °C points to the possible coexistence of relaxor ferroelectric regions as well. This observation is consistent with the identification of a pseudo-cubic phase in LaBi since relaxor ferroelectrics generally exhibit long-range pseudocubic symmetry. The general increase in ε_r at high temperatures/low frequencies is not related to the structural ferroelectric transformations but is instead attributed to an interfacial polarisation mechanism, which is associated with increasing electrical conductivity.[75]

In contrast, two distinct dielectric anomalies were observed in LaBa ceramics; the lower temperature anomaly occurred at a temperature T_1 in the range from 250 to 500 ˚C, while the Curie point occurred at a higher temperature, T_2, which was approximately 630 ˚C, as illustrated in Figure 4(b). The separation of chemically heterogeneous core and shell regions within the grains is the most obvious cause of such behaviour, with the distinct low- and high-temperature dielectric anomalies being a clear indicator of the dielectric responses in the shell and core regions respectively.[62,76] In this case, the lower-temperature peak at T_1 is related to the structural transformation of the shell consisting of a $BaTiO_3$-rich relaxor ferroelectric phase. On the other hand, the higher-temperature anomaly at T_2 can be attributed

View Article Online
DOI: 10.1039/C7TA09497C

to the Curie point of the $BiFeO_3$-enriched normal ferroelectric core. This proposal is generally consistent with the higher Curie temperature of $BiFeO_3$ (≈825 °C) in comparison with that of $BaTiO_3$ (≈130 °C). The frequency-dependence of the peak positions, together with the microstructural observations of $BiFeO_3$–rich core and $BaTiO_3$–rich shell regions, also points to this explanation of the dielectric behaviour. The diffuse phase transition and relaxor ferroelectric character is usually attributed to compositional heterogeneity on the nano-scale due to the existence of multiply charged ions in the ABO_3 structure, represented here by Bi^{3+}, Ba^{2+}, and La^{3+} on the A-site. This relaxor-like diffuse behaviour is also in good agreement with previous reports of diffuse phase transitions in xBiFeO$_3$–(1-x)BaTiO$_3$ ceramics with low $BiFeO_3$ contents (x<0.70).[33,69,77,78]

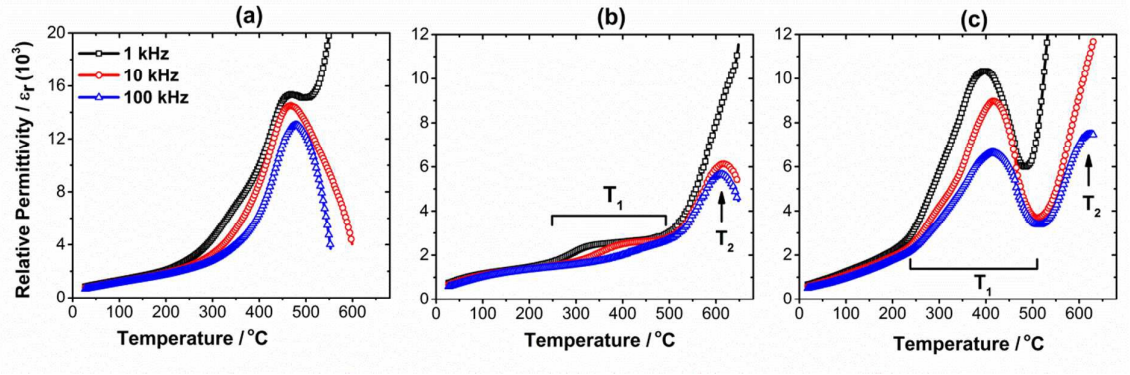

Figure 4. ε_r–T relationships for **a)** LaBi, **b)** LaBa and **c)** quenched-LaBa, measured at various frequencies.

In the case of the quenched-LaBa, it is apparent that the thermal quenching had a profound effect on the ε_r–T relationship, particularly in the region around the lower-temperature anomaly at T_1. The intensity of this peak increased remarkably, while simultaneously the frequency-dependence was reduced. The peak in permittivity at T_2 was affected less, although it became indistinct at lower frequencies due to increasing conductivity. The essential difference, in comparison with the as-sintered LaBa ceramic, is that the shift in peak position with frequency in the region around T_1 was relatively small, indicating that the characteristic relaxor-like behaviour in the shell was diminished. Thus, it is evident that the transformation from short-range polar nanoregions to long-range ordered ferroelectric domains was achieved by thermal quenching. This is also in agreement with the observation of increased rhombohedral phase fraction by structural analysis (Figure 3(c) and Table 1) and the relatively higher domain concentrations on the etched sections, as illustrated in Figure 1(c).

Similar observations concerning the influence of cooling rate on the temperature-dependent dielectric properties of 75BFBT were reported recently by Kim[48] It was suggested that a sequence of structural transformations occurred during heating, from rhombohedral (*R3c*) to ferroelectric orthorhombic (*Amm2*) near T_1 and then to cubic (*Pm-3m*) above T_2. The influence of oxygen vacancies on rhombohedral distortion was speculated to explain such transformations, although the occurrence of chemical heterogeneity and/or nano-scale phase segregation, as proposed in the present study, was not considered.

View Article Online
DOI: 10.1039/C7TA09497C

3.4 Ferroelectric Properties

Most reports on unmodified $BiFeO_3$-$BaTiO_3$ ceramics show that ferroelectric (P-E) hysteresis loops tend to display rounded features, indicating poor insulation behaviour and high dielectric loss.[27,79] Highly saturated hysteresis loops in modified 75BFBT compositions have been reported in several studies.[27,80,81] In the present work, rounded P-E loops were also recorded for the undoped composition (see the Figure S1c), but these were successfully transformed into well-saturated loops with a high remanent polarisation, $P_r \approx 0.27$ C m^{-2}, via the isovalent substitution of La^{3+} for Bi^{3+}, as illustrated in Figure 5(a). Current density (J-E) switching curves also clearly show that the reversal of polarisation occurred on exceeding the coercive field, E_c, of 4.1 kV mm^{-1}.

In contrast, the P-E loops of the LaBa ceramics exhibit a pinched, or constricted, shape (Figure 5(b)). Previous studies have attributed this type of constrained ferroelectric switching to the presence of antiferroelectric phases,[82,83] domain wall pinning by oxygen vacancy-cation dipolar defects,[84,85] or reversible electric field-induced relaxor to normal ferroelectric transformations.[86] The constricted loops observed in unmodified $BiFeO_3$ ceramics were attributed to domain wall pinning by defect dipoles.[87,88] In the present case, it was found that the P-E loop characteristics did not change significantly over time under the application of a continuous AC electric field with an amplitude of 8 kV mm^{-1} i.e. there was no evidence of field-forced 'de-ageing' effects that might indicate the occurrence of a dipolar defect-related domain stabilisation mechanism.

As an alternative mechanism, we propose that ferroelectric domain switching in the ferroelectric core regions within the LaBa ceramics is constrained by the *ergodic* relaxor ferroelectric nature of the shell regions, within which the polar nanoregions are unable to form long range-ordered ferroelectric domains under the influence of the electric field. The saturation polarisation, $P_S \approx 0.15$ C m^{-2}, is relatively high while the remanent polarisation, $P_r \approx 0.02$ C m^{-2}, is extremely low, indicating that the electric field-induced polarisation is unstable. The J-E curves do not show distinct current switching peaks, suggesting the continuous suppression of ferroelectric domain switching over a wide range of electric field. Thus, the constricted P-E loops in LaBa ceramics are attributed to the heterogeneous switching characteristics in the core and shell regions and the elastic coupling between them.

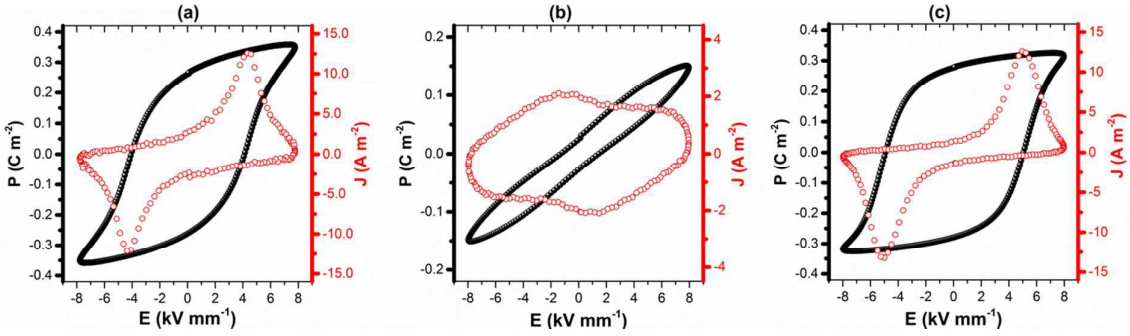

Figure 5. Ferroelectric (P-E) hysteresis loops and Leakage current density (J-E) curves of **a)** LaBi, **b)** LaBa and **c)** quenched-LaBa measured at room temperature.

View Article Online
DOI: 10.1039/C7TA09497C

Constricted P-E hysteresis loops have also been reported recently in rare earth-doped $BiFeO_3$ ceramics and thin films.[82,89–91] It was proposed that this behaviour is associated with the coupling/competition (electric-field induced phase transition) between non-polar/anti-polar *Pnma/Pbam* and polar *R3c* phases under the application of a high electric field. It is reported that incommensurate phases help to bridge the transformations between non-polar and polar phases, for compositions near to the morphotropic phase boundary for certain levels of rare-earth doping, which results in enhanced electromechanical properties. On the other hand, it was found that doping with La^{3+} hinders the nanoscale phase formation, due to the similarity of its ionic radius with that of Bi^{3+}.[90] Similar to the present case, chemically heterogeneous phases were also found as Bi-rich rhombohedral and Sm-rich orthorhombic phases in Sm-doped $BiFeO_3$, but at the nano scale.[91] Core-shell type microstructures have generally gained greater attention recently in Bi-based ferroelectrics, due to their potential for tailoring the ferroelectric and electro-mechanical properties through microstructural engineering.[64,76,92] The critical role of the core-shell interface was emphasised by Liu, who studied the coupling between the relaxor ferroelectric shell and ordered ferroelectric core regions in $0.75Bi_{1/2}Na_{1/2}TiO_3$-$0.25SrTiO_3$ ceramics.[93]

The use of rapid cooling or thermal quenching procedures has been widely reported as an effective method to enhance the ferroelectric switching behaviour of $BiFeO_3$-based ceramics, although the mechanisms involved are not well-understood.[48,87,94] The influence of such treatment on the ferroelectric domain switching behaviour of the LaBa ceramic is illustrated by the results presented in Figure 5(c). It is apparent that the quenching procedure greatly improved the polarisation switching characteristics of the LaBa composition, increasing the P_r value from 0.02 to 0.28 C m^{-2}. Sharp peaks in the J-E curves near 5 kV/mm also confirm the well-defined switching characteristics. The P_r values of the as-sintered LaBi and the quenched LaBa ceramics were similar, while the P_r/P_s ratio of the quenched-LaBa was somewhat higher than that of the as-sintered LaBi ceramic (0.86 compared with 0.75). This indicates that the ferroelectric domains show a highly irreversible character after the removal of the electric field. On the other hand, the coercive field of the quenched-LaBa was higher than that of LaBi (5 kV mm^{-1} compared with 4.1 kV mm^{-1}).

The occurrence of a constricted P–E loop with high saturation polarisation, P_s, and low remanent polarisation, P_r, for LaBa ceramics led us to investigate its energy storage properties. Figure 6(a) shows the P-E loops measured up to 10 kV mm^{-1} at room temperature. The stored energy density, W_{Stored} and energy loss, W_{Loss}, are shown graphically in Figure 6(b) on the quadrant of the P–E loop associated with the charging and discharging polarisation cycle (i.e increasing and decreasing electric field, E, respectively). In this case, the value of W_{Stored} at a given maximum electric field level was determined by numeric integration of the P-E data according to $W_{Stored} = \int_{Pr}^{Ps} E\, dP$. The energy storage density was found to be approximately 0.61 J cm^{-3} at 10 kV mm^{-1} which is comparable to those reported for other bismuth–barium–titanate[95–97] –niobate[98] and –ferrite[51,99] ceramics, which are generally in the range of 0.5 to 0.9 J cm^{-3} under a maximum field of ≈10 kV mm^{-1}.

View Article Online
DOI: 10.1039/C7TA09497C

One of the key factors to optimise the energy storage density in a dielectric material is to increase dielectric breakdown strength (DBS). It has been found that DBS can be increased by the reduction of grain size[98,100,101] or by the development of core-shell type microstructure[102,103] in ceramic materials. As recently reported[99] by Mishra, the DBS and energy storage density can be significantly increased using spark plasma sintering (SPS) instead of conventional ceramics processing in a $BiFeO_3$-based ceramics (W_{rec} >1 J cm^{-3}). On the other hand, recent modelling carried out by Wu[104] has revealed that the energy storage density can be improved in core-shell type microstructures. It was proposed that with the presence of the shell (non-polar or non-hysteric), the hysteresis loops become slanted, resulting in a decrease in energy loss, W_{Loss}. The underlying mechanism is attributed to improved homogeneity of the local electric field distribution due to the presence of the shell and therefore the dielectric nonlinearity is weakened, which favours high energy storage performance.

Based on our results for the slow-cooled LaBa ceramics, it is evident that the observed high energy storage density is likely related to the presence of the core-shell type grain formations with the evidence of pseudocubic phase in the shell, which reduces dielectric nonlinearity and hysteresis. Enhanced energy storage density in core-shell type microstructures has been also experimentally reported in $BaTiO_3$-$BiScO_3$ and $BaTiO_3$-$SrTiO_3$.[102,105] It was also suggested that the key aspect for optimising energy storage density is to control the volume of the shell phase[104]. Future investigations for these types of ceramics could assess the influence of modified processing procedures to optimise the performance of the shell and/or reduce the grain size to the sub-micron range.

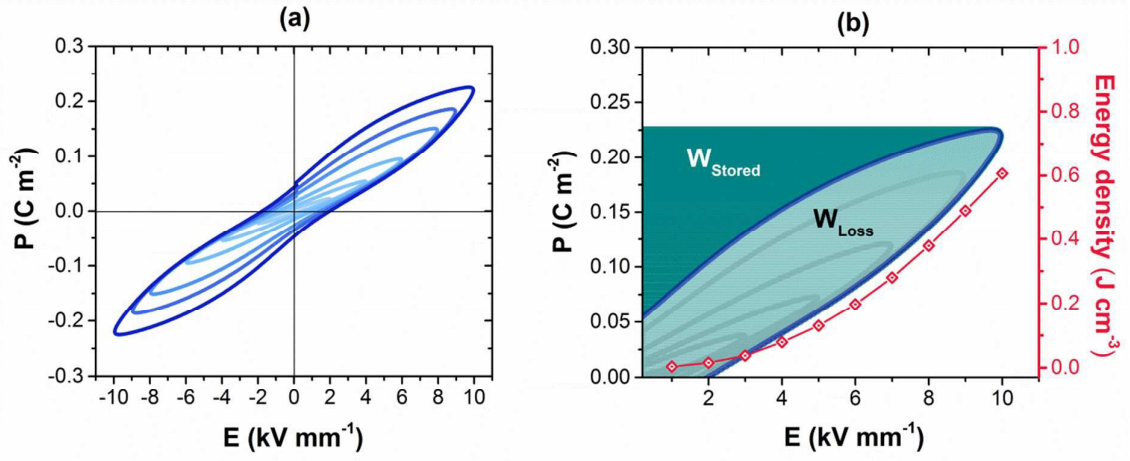

Figure 6. a) Ferroelectric (P-E) hysteresis loops for LaBa ceramics with various maximum electric field levels and **b)** quadrant of the P–E loop with the illustration of stored energy density, W_{Stored} and energy loss, W_{Loss}.

The results presented in sections 3.1 to 3.4 above can be evaluated to elucidate the mechanisms responsible for the observed enhancement in ferroelectric switching behaviour for the LaBa ceramics by air-quenching. Firstly, the observation of micro-scale ferroelectric domains throughout the grains in the quenched-LaBa ceramics (Figure 1(c)), in contrast to

View Article Online
DOI: 10.1039/C7TA09497C

the more clearly-defined core and shell regions in the slow-cooled specimen (Figure 1(b), indicates the development of improved ferroelectric ordering within the shell after quenching. The presence of coexisting rhombohedral and cubic, or perhaps more correctly pseudo-cubic, phases was identified using the SXPD patterns presented in Figure 3. In these results, it is apparent that the effect of quenching was to increase the proportion of the ferroelectric rhombohedral phase, which can be correlated generally with the changes in microstructure. However, we should also recognise that the pseudo-cubic phase, which is ascribed to the shell regions, has a relaxor ferroelectric character and may contain polar nanoregions (PNRs) with local non-cubic symmetry.

Evidence from the dielectric and ferroelectric properties of the quenched LaBa ceramics indicates that the shell regions are actually well-ordered and make strong contributions both to the lower-temperature dielectric peak at T_1 and the highly irreversible ferroelectric switching behaviour. Based on the latter results, it seems likely that the quenching procedure could have the effect of reducing the compositional fluctuations in the shell regions and thereby induces a transformation from an *ergodic* to *non-ergodic* relaxor ferroelectric state at room temperature. Further investigations were conducted using *in-situ* x-ray diffraction in order to test this hypothesis, as described in the next section.

3.5 In-situ X-ray Diffraction Studies

The influence of an applied electric field on the XRD patterns of the La-modified 75BFBT ceramics is illustrated by the pseudo-cubic $\{111\}_p$, $\{200\}_p$ and $\{220\}_p$ peak profiles presented in Figure 7. In comparison with the previous results described in section 3.2 above, these patterns were obtained from the bulk sintered ceramics (not crushed powders) and measured using high energy x-rays. This method provides a true indication of the average 'bulk' structure in the solid and enables the influence of the grain orientation relative to the electric field direction to be assessed. By this means, the development of preferred orientation and the associated lattice strain due to ferroelectric domain switching can be readily assessed. For the results presented in Figure 7, the patterns correspond to the 'families' of grains oriented with their scattering vectors parallel to the applied electric field direction i.e. for $\psi=0°$.

The diffraction peaks obtained by high energy XRD are generally broader than those obtained using high resolution SXPD, which hinders the identification of separate contributions from the rhombohedral core and pseudo-cubic shell regions. Nevertheless, by considering the changes in the peak profiles as a result of the applied electric field and grain orientation it is possible to deduce the main features of the underlying domain switching mechanisms. The influence of the applied electric field can be seen most readily in the $\{111\}_p$ peak profile for the quenched-LaBa ceramic (Figure 7(c)), where a pronounced shift of the peak occurs toward lower angles, accompanied by the development of a shoulder on the high-angle side. Qualitatively, this observation indicates the development of a large tensile strain in the pseudo-cubic (shell) region on application of the electric field. Ferroelectric domain switching within the core could also be occurring, but the associated

View Article Online
DOI: 10.1039/C7TA09497C

changes in the relative intensities of the $(111)_{CO}$ and $(\bar{1}11)_{CO}$ diffraction peaks of the rhombohedral phase are largely masked by overlap with the $(111)_{SH}$ and $(\bar{1}11)_{SH}$ peak of the shell.

The patterns recorded during and after application of the field for quenched-LaBa are similar, indicating that the field-induced strain is largely irreversible and therefore could be due to a form of ferroelectric domain switching rather than pure lattice strain. Compositional gradients and small structural distortions could contribute to broadening of the $(111)_C$ diffraction peak, which may mask the true nature of this 'lattice strain'. Nevertheless, the active nature of the shell regions in the quenched LaBa ceramics is clearly evident. Further observations of the $\{111\}_p$ peak shifts, presented in the lower part of Figure 7 as surfaces and contour plots, illustrate the responses to the cyclic electric field and highlight the much higher field-induced strain levels achieved for quenched-LaBa in comparison with the as-sintered LaBi and LaBa ceramics.

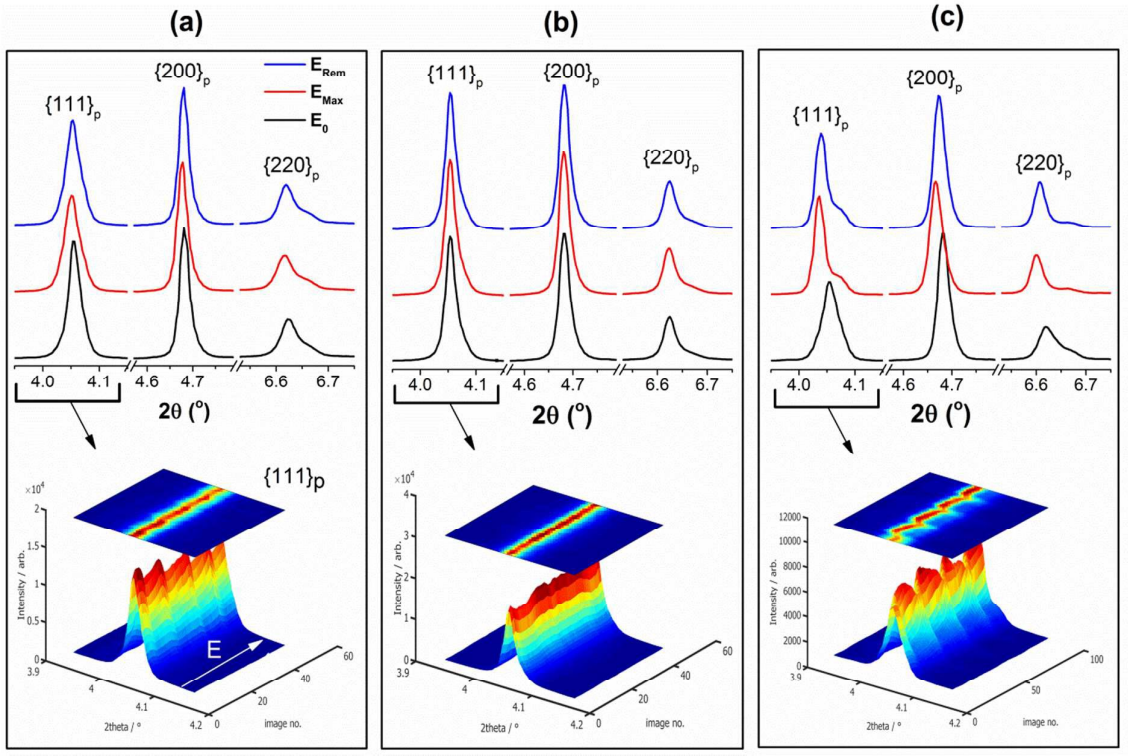

Figure 7. Variations in diffraction peak profiles for {111}, {200} and {220} along the field direction (ψ=0°) for **a)** LaBi, **b)** LaBa, and **c)** quenched-LaBa ceramics prior to application of the electric field (E_0), under a maximum electric field of 5 kV/mm (E_{Max}) and in the remanent state after removal of the electric field (E_{Rem}). The lower figures illustrate the responses of the $\{111\}_p$ peak profiles to the 2 bipolar electric field cycles.

The underlying mechanisms responsible for the electric field-induced strain in the quenched-LaBa ceramics can be clarified by inspection of the $\{111\}_p$ peak profiles, as illustrated in Figure 8(a). While the initial peak at zero electric field is broad, suggesting the presence of several overlapped peaks corresponding to the core and shell phases, the application of the electric field resulted in the suppression of the main peak at 4.065° and the growth of a new

View Article Online
DOI: 10.1039/C7TA09497C

dominant peak at 4.04°. It was initially felt that the apparent shift in this peak was associated with the intrinsic lattice strain of a pseudo-cubic shell phase. However, it seems more likely that the abrupt shift in position for an electric field above 3 kV mm^{-1} is actually associated with domain switching in a long range-ordered ferroelectric phase.

The irreversible nature of the peak shift, together with the high remanent polarization reported above for quenched-LaBa (Figure 5(c)), suggest that the evolution of the $\{111\}_p$ peak profile under an electric field is dominated by variations in the relative intensities of the $(111)_{SH}$ and $(\bar{1}11)_{SH}$ peaks (using pseudo-cubic indices), which indicates the occurrence of ferroelectric domain switching in the shell regions. The implication of these observations is that the shell regions in the quenched-LaBa ceramics are in a *non-ergodic* relaxor ferroelectric state and are transformed into ordered ferroelectric domains having rhombohedral symmetry under the influence of the electric field. The $(111)_{CO}$ and $(\bar{1}11)_{CO}$ peaks associated with the core regions are more widely separated due to the higher rhombohedral distortion of the $BiFeO_3$-rich phase and do not exhibit such clear indications of domain switching, although this is masked by overlap with the more dominant $(111)_{SH}$ and $(\bar{1}11)_{SH}$ peaks.

In the remanent state (Figure 8(b)), the changes in the relative intensities of the $(111)_{SH}$ and $(\bar{1}11)_{SH}$ peaks as a function of the azimuthal angle, ψ, are a direct indication of the preferred orientation of ferroelectric domains after poling under an electric field of 5 kV mm^{-1}. The invariance in the positions of the $(111)_{SH}$ and $(\bar{1}11)_{SH}$ peaks provides further evidence that the apparent shift in peak position is caused by variations in the relative intensities of these peaks due to domain switching rather than lattice strain in a single pseudo-cubic peak. Similar observations were made previously in the analysis of lattice strain and ferroelectric domain orientation distributions in poled rhombohedral PZT ceramics.[106]

View Article Online
DOI: 10.1039/C7TA09497C

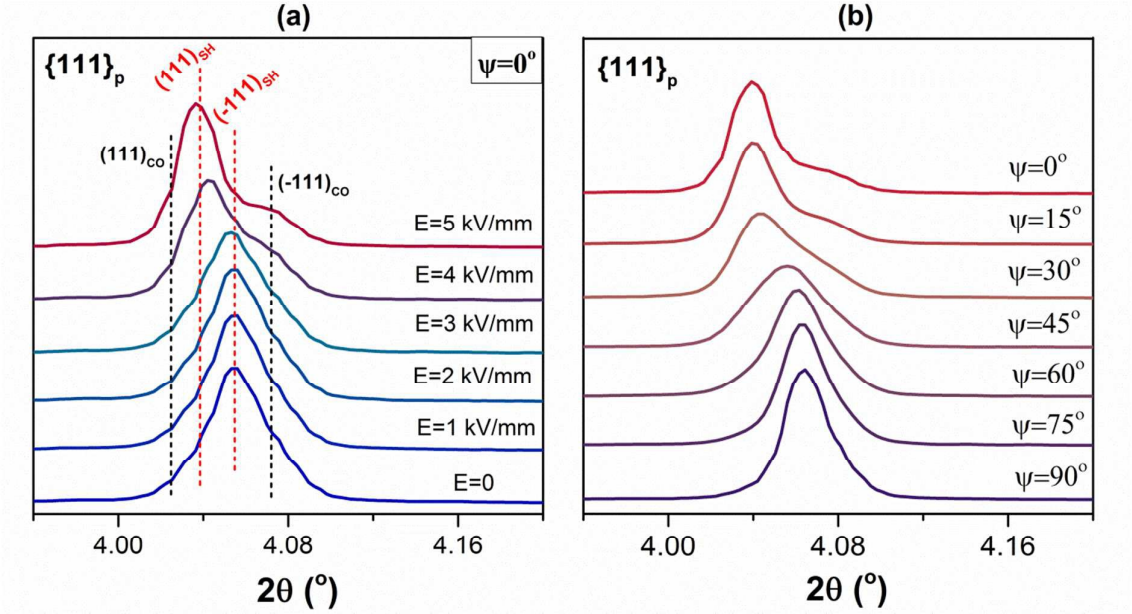

Figure 8. Changes in $\{111\}_p$ peak profiles for quenched-LaBa ceramic due to **(a)** increasing electric field and **(b)** grain orientation after poling. Dashed lines in (a) indicate the variations in the intensity of (111) and $(\bar{1}11)$ peaks due to ferroelectric domain switching in core and shell regions.

The anisotropy in electric field-induced strain, taking into account both the *intrinsic* lattice strain and the *extrinsic* transformation strain due to domain switching, was quantified by determining the weighted-average peak positions, which were then converted into effective average lattice spacings, d_{hkl}, for several different crystallographic orientations. To accomplish this, peak profile fitting was carried out using a Pseudo-Voigt function within Matlab. The effective field-induced lattice strain associated with each reflection, ε_{hkl}, was then calculated from the initial d-spacing, $d_{hkl}(0)$, as follows:

$$\varepsilon_{hkl}(E) = \frac{d_{hkl}(E) - d_{hkl}(0)}{d_{hkl}(0)}$$

The influence of the applied electric field on the weighted-average lattice strains for the $\{111\}_p$, $\{200\}_p$ and $\{220\}_p$ orientations in quenched-LaBa is illustrated by the results presented in Figure 9(a). The variations in strain can be correlated with the applied electric field, which underwent 2 complete bipolar cycles with an amplitude of 5 kV mm^{-1}. For each orientation, the lattice strain increased sharply on exceeding the coercive electric field around 3 kV mm^{-1} and then underwent a sequence of hysteretic variations in response to the ferroelectric domain switching events. The lattice strains parallel to the electric field direction, for $\psi = 0°$, were generally positive (tensile) while those in the transverse direction, $\psi = 90°$, were negative (compressive). This behaviour is consistent with the changes in macroscopic strain that result from poling polycrystalline ferroelectric ceramics.[106]

Although the effective lattice strains associated with different crystallographic orientations were generally correlated together, their magnitudes were strongly heterogeneous, with the

View Article Online
DOI: 10.1039/C7TA09497C

values decreasing in the order $\varepsilon_{\{111\}} > \varepsilon_{\{220\}} > \varepsilon_{\{200\}}$. For example, under an electric field level of 5 kV mm^{-1} the lattice strains were recorded as ε_{111}=0.48%, ε_{220}=0.35% and ε_{200}=0.33%. This result supports the suggestion that the crystal structure of the active shell region is rhombohedral, since the largest transformation strains occur by ferroelectric domain switching along the polar <111> directions.

The macroscopic strain was estimated based on the weighted average of the effective lattice strains associated with different crystallographic orientations, according to equation shown below[54,107]

$$\varepsilon(\Psi) = \frac{\sum_{hkl} T_{hkl}\, m_{hkl}\, \varepsilon_{hkl}(\Psi)}{\sum_{hkl} T_{hkl}\, m_{hkl}}$$

where $\varepsilon(\psi)$ is the component of the macroscopic strain tensor for a given orientation, $\varepsilon_{hkl}(\psi)$ is the local lattice strain along the axis parallel to direction ψ for the *{hkl}* orientation, T_{hkl} is the texture index, and m_{hkl} is the multiplicity of the reflection for *{hkl}* planes. This expression relies on the assumption of isotropic elasticity at the local scale, so that it is expected to give only indicative values.[54] Treating the material as cubic and with random grain texture, T_{hkl} reduces to 1 for any *hkl*, and m_{hkl} is 8, 6, and 12 for {111}, {200}, and {220} orientations, respectively.

The calculated macroscopic strains both parallel and perpendicular to the electric field direction, corresponding to ψ=0˚ and ψ=90˚ respectively, are presented in Figure 9(b). It can be seen that high field-induced strains, $\varepsilon(0^\circ)\approx 0.4\%$ and $\varepsilon(90^\circ)\approx 0.18\%$ at 5 kV mm^{-1}, were obtained for quenched-LaBa. Well-defined butterfly-type strain-field hysteresis loops were obtained, which are similar to those reported for other ferroelectric ceramic materials. In contrast, only a weak electrostrictive response was recorded for the as-sintered LaBa due to the lack of well-ordered ferroelectric domains in the shell regions. Isovalent substitution of La^{3+} in Bi^{3+} in the LaBi ceramics, without thermal quenching also yielded butterfly-type strain-field curves, but with a substantial reduction in magnitude relative to those of the quenched-LaBa. These results indicate that the application of a quenching procedure is vital to optimise the electromechanical properties of La-modified BF-BT ceramics. It seems likely that some nanoscale chemical heterogeneity could also be present in the as-sintered LaBi ceramic, in view of the relatively low electromechanical response in comparison with the quenched LaBa material.

View Article Online
DOI: 10.1039/C7TA09497C

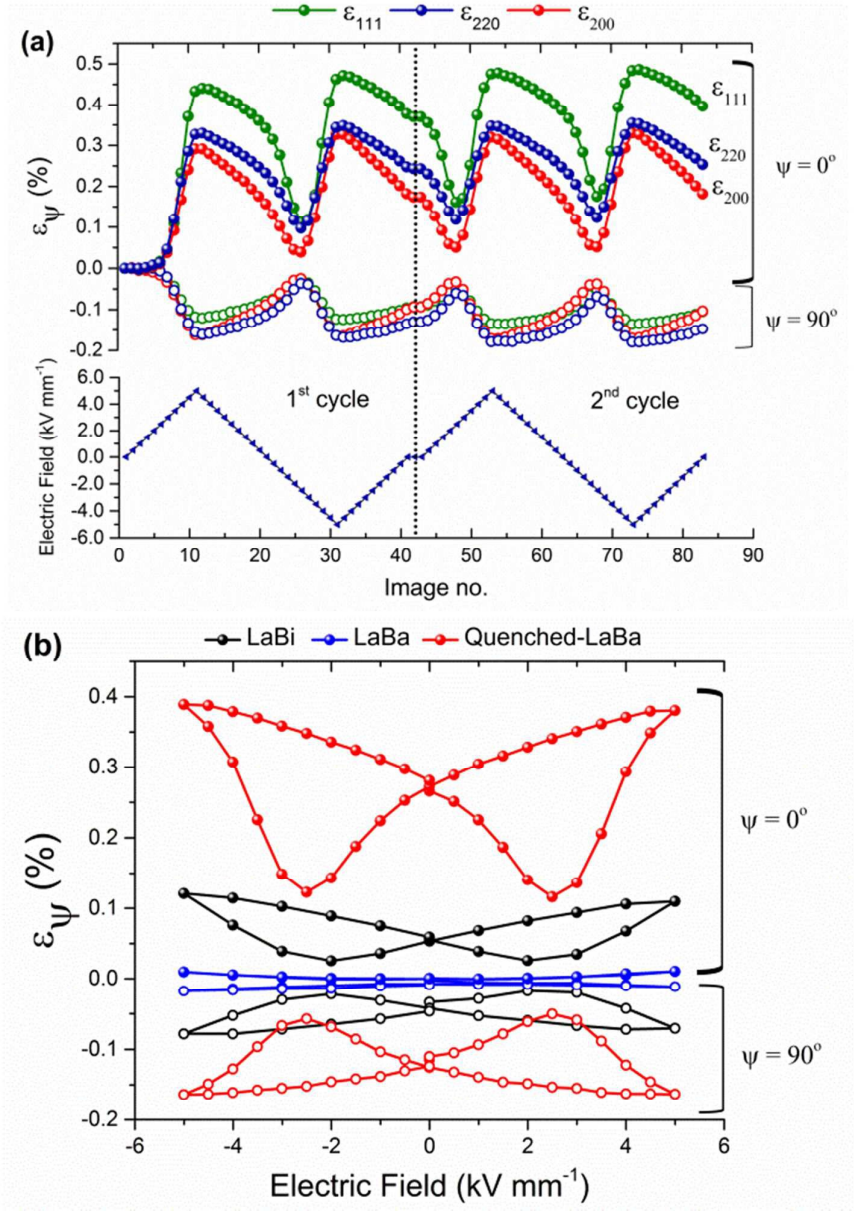

Figure 9. a) Microscopic lattice strain contrubitons of {111}, {200} and {220} for quenched-LaBa at Ψ=0˚ and Ψ=90˚. **b)** Macroscopic strain curves of all compositions at ψ=0˚ and ψ=90˚. Note that error bars are smaller than the marker size.

After 2 bipolar cycles shown above, the ceramics were subjected to a unipolar cycle to determine their effective piezoelectric coefficients, d_{33}^{ef} and d_{31}^{ef} (see Figure S4). It was found that the d_{33}^{ef} and d_{31}^{ef} values were 87 and -81 pm V^{-1} for LaBi, 207 and -100 pm V^{-1} for quenched-LaBa, respectively. These results are comparable with those derived from macroscopic strain-field measurements on other BF–BT ceramics in the as-sintered[27,32] or water-quenched[9,108] state. It is anticipated that the piezoelectric activity would be improved for BF–BT compositions closer to the MPB at around 67% BF.

View Article Online
DOI: 10.1039/C7TA09497C

3.6 Magnetic Properties

The magnetic (M-H) hysteresis loops of the investigated compositions measured at room temperature, including the undoped 75BFBT, are illustrated in Figure 10. The hysteresis loop of undoped 75BFBT shows a very low but non-zero remanent magnetisation (0.0075 emu/g), indicating the canted antiferromagnetic behaviour (i.e. slightly canted antiparallel alignment of Fe^{3+} spins) which is likely due to occupancies of Ba^{2+} and Ti^{4+} in the $BiFeO_3$ matrix.[33,77] It is well-known that $BiFeO_3$ is G-type antiferromagnetic implying that the alignment of neighbouring Fe magnetic moments is antiparallel.[4] Therefore, the key to enhance the ferromagnetism in $BiFeO_3$ is to disrupt the intrinsic spiral spin structure through foreign ion substitution, as reported previously.[13,109–111]

In the present case, a small amount of La substitution at the A-site effectively increased the ferromagnetic moment, even though the substituent ion is known to be diamagnetic.[13] It can be noticed that the loops are not fully saturated under an applied magnetic field of 20 kOe. However, weak ferromagnetic moments with remanent magnetisation, M_r, values of 0.17, 0.12 and 0.042 emu/g were obtained for LaBi, LaBa, and quenched-LaBa, respectively. It is evident that M_r was increased by isovalent substitution of La^{3+} for Bi^{3+}, whilst it was decreased by donor substitution of La^{3+} for Ba^{2+}. Since the chemical heterogeneity and structural distortion in LaBi was not as pronounced as that in LaBa, the increase of M_r (relative to the unmodified 75BFBT) could be due to disruption of the spatially modulated spin cycloidal structure of the $BiFeO_3$ matrix. However, the micro-segregation of $BiFeO_3$-rich and -depleted regions in the form of core-shell type grain structures makes the interpretation of the loops more complicated for the LaBa ceramics.

It has been shown that the ferromagnetic properties of $BiFeO_3$-based multiferroics are dramatically influenced by structural defects[109,112]. Indeed, even small deviations from the ideal cation–anion stoichiometry can induce the formation of lattice defects, which interfere with the antiferromagnetic ordering and lead to weak ferromagnetic behaviour.[24,109,112] The observation of weak ferromagnetism with a substantial reduction in the magnetic coercive field, H_C, for the as-sintered LaBa in comparison with LaBi could be associated with higher defect populations in the donor-type LaBa. The occurrence of core-shell grain microstructures with poor ferroelectric switching behaviour and relaxor ferroelectric character in the shell regions for the as-sintered LaBa ceramics provides qualitative evidence for nanoscale phase segregation within the shell or at the interface.

For the case of quenched-LaBa, it can be observed that M_r was significantly reduced after thermal quenching. The cause of this reduction could be associated with changes in the oxygen vacancy concentrations, since it is anticipated that thermal quenching might 'freeze-in' a higher concentration of oxygen vacancies than that of the as-sintered material.[113] On the other hand, the influence of quenching on chemical heterogeneity in the shell regions, which has already been linked to dramatic improvements in the ferroelectric switching behaviour, could provide a more likely explanation for the reduction in M_r. Improvements in ferroelectric properties accompanied by weak ferromagnetic behaviour were also reported by Zhang, who studied the effects of quenching on $BiFeO_3$.[68] Further investigations involving

View Article Online
DOI: 10.1039/C7TA09497C

high resolution TEM and Magnetic Force Microscopy are required to confirm the nature of such nanoscale defects and their influence on magnetic properties.

An additional factor that should always be taken into account when considering the origin of weak ferromagnetism in $BiFeO_3$-based ceramics is the presence of parasitic ferromagnetic phases such as Fe_2O_3 or Fe-enriched secondary phases forming during sintering. Close inspection of the high resolution SXPD data does not reveal any prominent secondary phases, although a high background in the patterns could hinder their observation. Nevertheless, small amounts of Fe-rich phases were detected in the LaBi ceramics (see the Figure S3). However the chemical composition of these phases could not be determined accurately by point analysis in SEM-EDS due to their small sizes and high Bi irradiation interfering with the signal collection. Based on previous reports on $BiFeO_3$-based ceramics[6,12,36,110], $Bi_2Fe_4O_9$ is a common Fe-rich secondary phase however it is paramagnetic. A small amount of unreacted Fe_2O_3 could also potentially be present, but its magnetic coercive field ($H_C \approx 100$ Oe) is very low compared to that found for LaBi ($H_C \approx 2700$ Oe).

A recent report by Khomchenko[109] provided similar observations of a Fe-rich phase in $Bi_{0.9}Ba_{0.1}Fe_{0.9}Ti_{0.1}O_3$, with the chemical composition being reported as Ti-doped $BaFe_{12}O_{19}$. It was suggested that there was a close correlation between the H_C of the detected secondary phase and the studied composition ($H_C \approx 3000$ Oe), similarly to the present case. Thus, the contribution of a ferromagnetic parasitic phase cannot completely be ruled out and the ferromagnetic properties of LaBi ceramics should be interpreted with due consideration for this possibility. On the other hand, further systematic studies on increasing La substitution for both Bi and Ba in 75BFBT showed a gradual increase in magnetisation, which was found to be moderately independent of grain size variation and chemical heterogeneity (see the supplementary Figure S5). Additional powder neutron diffraction studies[111] to investigate magnetic Bragg reflections would be useful to provide deeper understanding of the (anti)ferromagnetic nature of the studied compositions.

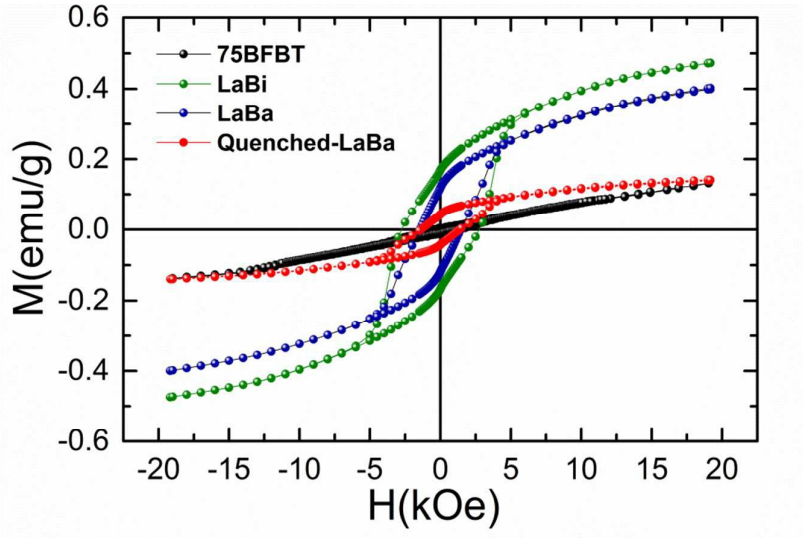

Figure 10. Ferromagnetic (M-H) hysteresis loops of undoped 75BFBT, LaBi, LaBa and quenched-LaBa measured at room temperature.

View Article Online
DOI: 10.1039/C7TA09497C

The changes in magnetoelectric (ME) coefficient α_{ME} as a function of the dc bias magnetic field H, measured at room temperature, for LaBi, LaBa and quenched-LaBa ceramics are presented in Figure 11(a). As the poling field increased from 0.15 to 3.5 kV mm^{-1}, α_{ME} for quenched-LaBa increased from 1.68 to 6.20 mV/cm Oe at 1 Tesla and from 1.98 to 7.40 mV/cm Oe at 7 Tesla. The influence of chemical composition and processing procedures shows a good general correlation with the ferroelectric behaviour and domain switching characteristics described in sections 3.4 and 3.5 respectively. The observation of a monotonic increase in α_{ME} with increasing magnetic field at low and high poling fields for all compositions indicates the coupling between polarisation and magnetisation. As the applied magnetic field increases, then deformation occurs due to the effect of magnetostriction, which couples to the polar phase through piezoelectricity. It has been suggested in many reports[114,115] that the ME properties could effectively be enhanced by constructing a composite comprising a ferromagnetic core coupled elastically to a piezo/ferroelectric shell. Thus, the higher ME coupling for the quenched-LaBa could be a consequence of its enhanced electro-mechanical strain and composite-like microstructure.

In the case of LaBa and quenched-LaBa, it was found that the core consists of a $BiFeO_3$-rich multiferroic phase while the shell is a $BaTiO_3$-rich relaxor or normal long-range ordered ferroelectric, depending on the cooling conditions (as-sintered or quenched state). As discussed in sections 3.4 and 3.5, ferroelectric switching in LaBa is restricted due to the relaxor ferroelectric nature of the shell, which results in a low ME interaction. However, it is apparent that that transformation of the shell component from PNRs to long-range ordered ferroelectric domains by thermal quenching could potentially have a profound effect on the bulk magnetoelectric coupling at room temperature, as shown in Figure 11(a), despite the lower saturation and remanent magnetisation values (Figure 10). Thus, the ME effect in such structures could be dependent on the coexistence of ferroelectric and multiferroic phases, as well as the elastic coupling between them.

The temperature dependencies of the ME coefficients, presented in Figure 11(b), show a maximum in α_{ME} around ≈320˚C for LaBi and ≈363˚C for both LaBa and quenched-LaBa. These maxima in the α_{ME}-T curves can be attributed to strong magnetoelectric ordering near the (anti)ferromagnetic phase transition at the Neel Temperature, T_N. It is interesting to note that the reported T_N value for single phase $BiFeO_3$ is ≈370˚C,[4] which is close to the observed transition points for LaBa and quenched-LaBa. It was shown previously that chemical heterogeneity, in the form of core-shell type microstructures, was persistent in both ceramics, regardless of the structural changes induced by quenching. Therefore, the magnetoelectric response is likely to arise mostly from the $BiFeO_3$–rich phase in the core regions. However, in the case of LaBi the lack of a clear core-shell structure leads to a more transformation with a reduced transition temperature, indicating that the distribution of the ferroelectric and (anti)ferromagnetic phases is more homogeneous. The reduction in T_N is consistent with previous reports on BF-BT ceramics.[77] Such transitions are sometimes correlated with anomalies in the dielectric properties of multiferroics such as $YMnO_3$,[116] $BiMnO_3$,[117] and $BiFeO_3$[4,118] and interpreted as evidence for magnetoelectric coupling. Thus, the remarkable increase in α_{ME} near T_N can be interpreted as a strong coupling between magnetic field and

View Article Online
DOI: 10.1039/C7TA09497C

the polarisation, which could contribute to the increased dielectric response in the vicinity of T_1 in the quenched-LaBa composition.

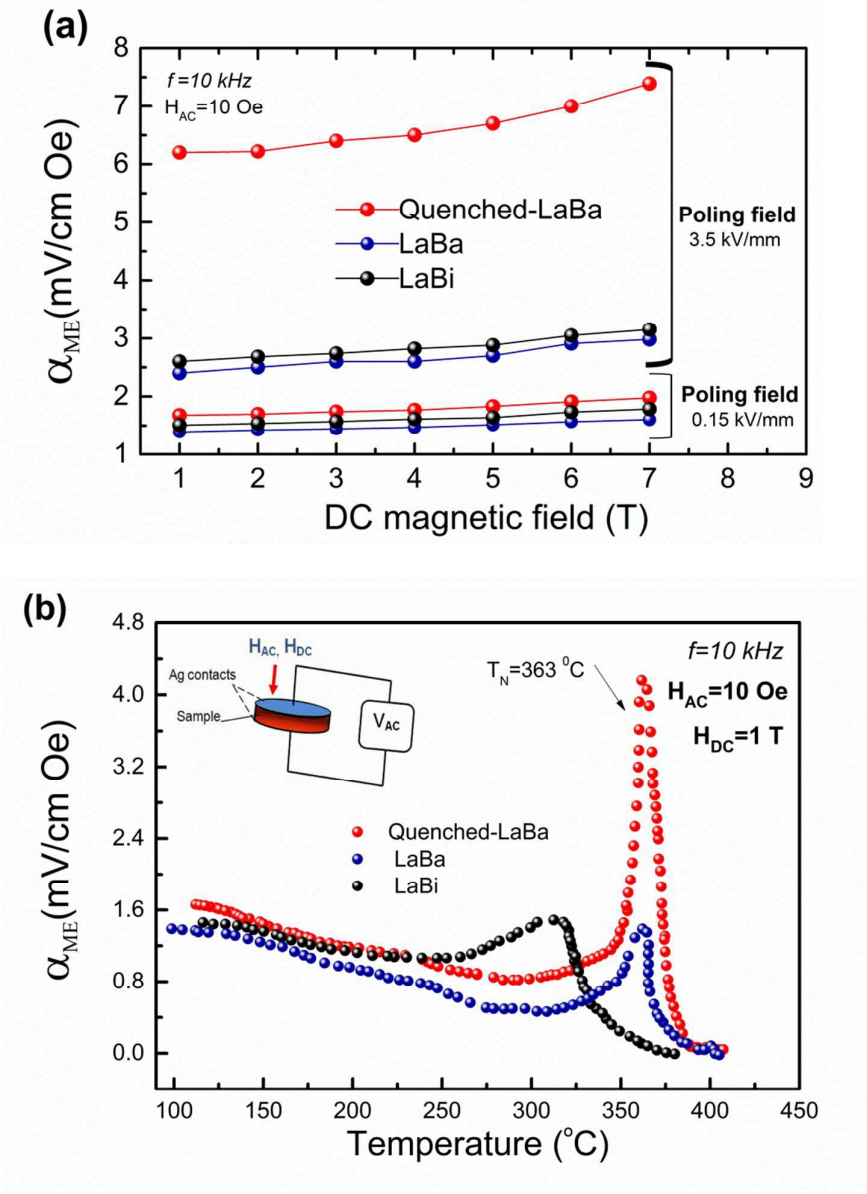

Figure 11. a) Variations in magnetoelectric voltage coefficient, α_{ME}, at poling fields of 0.15 and 3.5 kV mm^{-1} as a function of DC magnetic field at room temperature, **b)** α_{ME} as a function of temperature with a fixed magnetic field (poling field=0.15 kV mm^{-1}).

View Article Online
DOI: 10.1039/C7TA09497C

4. CONCLUSIONS

It has been shown that the microstructure development in 1 mol% La-doped $0.75BiFeO_3$-$0.25BaTiO_3$ (75BFBT) ceramics is strongly dependent on the dopant incorporation strategy, with isovalent substitution yielding relatively homogeneous large-grained structures and donor substitution leading to the formation of fine-grained core-shell type morphology. The ferroelectric switching behaviour in the donor-substituted ceramics was relatively constrained due to its relaxor ferroelectric character, yielding a dielectric energy storage density of 0.61 J cm^{-3} at an electric field of 10 kV mm^{-1}. Enhancement of the ferroelectric characteristics due to air-quenching was attributed to transformation of the pseudo-cubic ergodic relaxor shell phase into a rhombohedral non-ergodic state as a result of improved chemical homogeneity on the nanoscale. This supposition is supported by modifications in the dielectric permittivity-temperature relationships and investigations of the electromechanical actuation mechanisms using in-situ x-ray diffraction, which showed that the electric field-induced strain is dominated by ferroelectric domain switching in the shell regions. Magnetic measurements confirm the weak ferromagnetism in La-modified 75BFBT ceramics, which show significant variations in magnetisation and magnetoelectric properties depending on the processing methods.

Although the as-sintered donor-doped ceramics exhibit constrained ferroelectric switching characteristics, research into their composition-structure-property relationships may bring new insight into the multifunctional properties of $BiFeO_3$-based ceramics and nanocomposites. Additional studies exploring higher dopant levels, different BF/BT ratios, modified heat treatment procedures and nanoscale imaging would help to clarify the influence of the core-shell microstructures on magnetoelectric properties.

Acknowledgements

We thank Diamond Light Source for access to beamlines I11 (proposal number EE17673) and I15 (proposal number EE16390-1) that contributed to the results presented here. The assistance of Dr Stephen Thompson, Dr Claire Murray and Prof Chiu Tang is gratefully acknowledged. The authors are grateful to Dr Kamal G. Abdulvakhidov (Smart Materials Research Center Southern Federal University, Rostov-on-Done, Russia) for helping in magnetic measurements. Magnetic property investigations partially were supported by project "Phase transitions, magnetotransport, magnetocaloric, magnetoelectric phenomena in strongly correlated electron systems" (№ 0203-2016-0009). The authors thank Prof Ian M. Reaney (Department of Materials Science and Engineering, University of Sheffield, Sheffield, UK) and Dr Alexander Khort (A.V Luikov Heat and Mass Transfer Institute of National Academy of Sciences of Belarus, Minsk, Belarus) for helpful discussion. I. Calisir also thanks the National Education of Turkish Republic for financial support throughout his PhD programme.

View Article Online
DOI: 10.1039/C7TA09497C

5. REFERENCES

1. Rödel, J. *et al.* Transferring lead-free piezoelectric ceramics into application. *J. Eur. Ceram. Soc.* **35,** 1659–1681 (2015).

2. Hong, C.-H. *et al.* Lead-free piezoceramics – Where to move on? *J. Mater.* **2,** 1–24 (2016).

3. Rödel, J. *et al.* Perspective on the development of lead-free piezoceramics. *J. Am. Ceram. Soc.* **92,** 1153–1177 (2009).

4. Catalan, G. & Scott, J. F. Physics and applications of bismuth ferrite. *Adv. Mater.* **21,** 2463–2485 (2009).

5. Ortega, N., Kumar, A., Scott, J. F. & Katiyar, R. S. Multifunctional magnetoelectric materials for device applications. *J. Phys. Condens. Matter* **27,** 504002 (2015).

6. Rojac, T. *et al.* $BiFeO_3$ Ceramics: Processing, electrical, and electromechanical properties. *J. Am. Ceram. Soc.* **97,** 1993–2011 (2014).

7. Ibn-Mohammed, T. *et al.* Integrated hybrid life cycle assessment and supply chain environmental profile evaluations of lead-based (lead zirconate titanate) versus lead-free (potassium sodium niobate) piezoelectric ceramics. *Energy Environ. Sci.* **9,** 3495–3520 (2016).

8. Leontsev, S. O. & Eitel, R. E. Progress in engineering high strain lead-free piezoelectric ceramics. *Sci. Technol. Adv. Mater.* **11,** 044302 (2010).

9. Lee, M. H. *et al.* High-performance lead-free piezoceramics with high curie temperatures. *Adv. Mater.* **27,** 6976–6982 (2015).

10. Beuerlein, M. A. *et al.* Current understanding of structure-processing-property relationships in $BaTiO_3$-$Bi(M)O_3$ dielectrics. *J. Am. Ceram. Soc.* **99,** 2849–2870 (2016).

11. Wang, L., Yang, C.-H. & Wen, J. Physical principles and current status of emerging non-volatile solid state memories. *Electron. Mater. Lett.* **11,** 505–543 (2015).

12. Selbach, S. M., Einarsrud, M. & Grande, T. On the thermodynamic stability of $BiFeO_3$. *Chem. Mater.* **21,** 169–173 (2009).

13. Perejón, A. *et al.* Single phase, electrically insulating, multiferroic La-substituted $BiFeO_3$ prepared by mechanosynthesis. *J. Mater. Chem. C* **2,** 8398–8411 (2014).

14. Kumar, M. & Yadav, K. L. Rapid liquid phase sintered Mn doped $BiFeO_3$ ceramics with enhanced polarization and weak magnetization. *Appl. Phys. Lett.* **91,** 242901 (2007).

View Article Online
DOI: 10.1039/C7TA09497C

15. Suresh, P. & Srinath, S. Effect of synthesis route on the multiferroic properties of $BiFeO_3$: A comparative study between solid state and sol-gel methods. *J. Alloys Compd.* **649,** 843–850 (2015).

16. Reddy, V. R. *et al.* Reduced leakage current of multiferroic $BiFeO_3$ ceramics with microwave synthesis. *Ceram. Int.* **40,** 4247–4250 (2014).

17. Yang, C., Kan, D., Takeuchi, I., Nagarajan, V. & Seidel, J. Doping $BiFeO_3$: approaches and enhanced functionality. *Phys. Chem. Chem. Phys.* **14,** 15953–15962 (2012).

18. Walker, J. *et al.* Temperature dependent piezoelectric response and strain–electric-field hysteresis of rare-earth modified bismuth ferrite ceramics. *J. Mater. Chem. C* **4,** 7859–7868 (2016).

19. Zhang, L. & Yu, J. Residual tensile stress in robust insulating rhombohedral $Bi_{1-x}La_xFe_{1-y}Ti_yO_3$ multiferroic ceramics and its ability to pin ferroelectric polarization switching. *Appl. Phys. Lett.* **106,** 112907 (2015).

20. Uniyal, P. & Yadav, K. L. Pr doped bismuth ferrite ceramics with enhanced multiferroic properties. *J. Phys.Condens. Matter* **21,** 405901 (2009).

21. Trivedi, P. *et al.* Modifications in the electronic structure of rare-earth doped $BiFeO_3$ multiferroic. *Solid State Commun.* **222,** 5–8 (2015).

22. Arnold, D. C. Composition-driven structural phase transitions in rare-earth-doped $BiFeO_3$ ceramics : A review. *IEEE Trans. Ultrason. Ferroelectr. Freq. Control* **62,** 62–82 (2015).

23. Karimi, S., Reaney, I. M., Han, Y., Pokorny, J. & Sterianou, I. Crystal chemistry and domain structure of rare-earth doped $BiFeO_3$ ceramics. *J. Mater. Sci.* **44,** 5102–5112 (2009).

24. Bernardo, M. S. *et al.* Intrinsic compositional inhomogeneities in bulk Ti-doped $BiFeO_3$: Microstructure development and multiferroic properties. *Chem. Mater.* **25,** 1533–1541 (2013).

25. Azough, F. *et al.* Microstructure and properties of Co- , Ni- , Zn- , Nb- and W-modified multiferroic $BiFeO_3$ ceramics. *J. Eur. Ceram. Soc.* **30,** 727–736 (2010).

26. Freitas, V. F. *et al.* Structural phase relations in perovskite-structured $BiFeO_3$-based multiferroic compounds. *J. Adv. Ceram.* **2,** 103–111 (2013).

27. Leontsev, S. O. & Eitel, R. E. Dielectric and piezoelectric properties in Mn-modified (1-x)$BiFeO_3$–x$BaTiO_3$ ceramics. *J. Am. Ceram. Soc.* **92,** 2957–2961 (2009).

28. Lennox, R. C. *et al.* PZT-like structural phase transitions in the $BiFeO_3$–$KNbO_3$ solid solution. *Dalt. Trans.* **44,** 10608–10613 (2015).

View Article Online
DOI: 10.1039/C7TA09497C

29. Lin, D. *et al.* Microstructure, ferroelectric and piezoelectric properties of $Bi_{0.5}K_{0.5}TiO_3$-modified $BiFeO_3$–$BaTiO_3$ lead-free ceramics with high Curie temperature. *J. Eur. Ceram. Soc.* **33,** 3023–3036 (2013).

30. Yabuta, H. *et al.* Microstructure of $BaTiO_3$–$Bi(Mg_{1/2}Ti_{1/2})O_3$–$BiFeO_3$ piezoelectric ceramics. *Jpn. J. Appl. Phys.* **51,** 09LD04 (2012).

31. Sebastian, T. *et al.* High temperature piezoelectric ceramics in the $Bi(Mg_{1/2}Ti_{1/2})O_3$-$BiFeO_3$-$BiScO_3$-$PbTiO_3$ system. *J. Electroceramics* **25,** 130–134 (2010).

32. Wei, J., Fu, D., Cheng, J. & Chen, J. Temperature dependence of the dielectric and piezoelectric properties of $xBiFeO_3$–$(1-x)BaTiO_3$ ceramics near the morphotropic phase boundary. *J. Mater. Sci.* **52,** 10726–10737 (2017).

33. Kumar, M. M., Srinivas, A. & Suryanarayana, S. V. Structure property relations in $BiFeO_3$/$BaTiO_3$ solid solutions. *J. Appl. Phys.* **87,** 855–862 (2000).

34. Leontsev, S. O. & Eitel, R. E. Origin and magnitude of the large piezoelectric response in the lead-free $(1– x)BiFeO_3– xBaTiO_3$ solid solution. *J. Mater. Res.* **26,** 9–17 (2011).

35. Amorín, H. *et al.* Very high remnant polarization and phase-change electromechanical response of $BiFeO_3$ -$PbTiO_3$ at the multiferroic morphotropic phase boundary. *Appl. Phys. Lett.* **101,** 172908 (2012).

36. Valant, M., Axelsson, A. & Alford, N. Peculiarities of a solid-state synthesis of multiferroic polycrystalline $BiFeO_3$. *Chem. Mater.* **19,** 5431–5436 (2007).

37. Guo, Y. *et al.* Critical roles of Mn-ions in enhancing the insulation, piezoelectricity and multiferroicity of $BiFeO_3$-based lead-free high temperature ceramics. *J. Mater. Chem. C* **3,** 5811–5824 (2015).

38. Joo, H. W., Kim, D. S., Kim, J. S. & Cheon, C. I. Piezoelectric properties of Mn-doped $0.75BiFeO_3$−$0.25BaTiO_3$ ceramics. *Ceram. Int.* **42,** 10399–10404 (2016).

39. Calisir, I. & Hall, D. A. Chemical heterogeneity and approaches to its control in $BiFeO_3$–$BaTiO_3$ lead-free ferroelectrics. *J. Mater. Chem. C* **6,** 134–146 (2018).

40. Wang, D. *et al.* Temperature dependent, large electromechanical strain in Nd-doped $BiFeO_3$-$BaTiO_3$ lead-free ceramics. *J. Eur. Ceram. Soc.* **37,** 1857–1860 (2017).

41. Zhou, C. *et al.* Dielectric, ferroelectric and piezoelectric properties of La-substituted $BiFeO_3$–$BaTiO_3$ ceramics. *Ceram. Int.* **39,** 4307–4311 (2013).

42. Yu, B. *et al.* Effects of ion doping at different sites on electrical properties of multiferroic $BiFeO_3$ ceramics. *J. Phys. D. Appl. Phys.* **41,** 065003 (2008).

43. Culver, S. P., Stepanov, V., Mecklenburg, M., Takahashi, S. & Brutchey, R. L. Low temperature synthesis and characterization of lanthanide-doped $BaTiO_3$ nanocrystals. *Chem. Commun.* **50,** 3480 (2014).

View Article Online
DOI: 10.1039/C7TA09497C

44. Makovec, D., Samardzija, Z., Delalut, U. & Kolar, D. Defect structure and phase relations of highly lanthanum-doped barium titanate. *J. Am. Ceram. Soc.* **78,** 2193–2197 (1995).

45. West, A. R., Adams, T. B., Morrison, F. D. & Sinclair, D. C. Novel high capacitance materials: $BaTiO_3$:La and $CaCu_3Ti_4O_{12}$. *J. Eur. Ceram. Soc.* **24,** 1439–1448 (2004).

46. Castro, M. S., Salgueiro, W. & Somoza, A. Electron paramagnetic resonance and positron annihilation study of the compensation mechanisms in donor-doped $BaTiO_3$ ceramics. *J. Phys. Chem. Solids* **68,** 1315–1323 (2007).

47. Liu, N. *et al.* Large remanent polarization and enhanced magnetic properties in non-quenched $Bi(Fe,Ga)O_3$-$(Ba,Ca)(Zr,Ti)O_3$ multiferroic ceramics. *Appl. Phys. Lett.* **110,** 112902 (2017).

48. Kim, D. S., Cheon, C. Il, Lee, S. S. & Kim, J. S. Effect of cooling rate on phase transitions and ferroelectric properties in $0.75BiFeO_3$-$0.25BaTiO_3$ ceramics. *Appl. Phys. Lett.* **109,** 202902 (2016).

49. Kim, S. *et al.* Revealing the role of heat treatment in enhancement of electrical properties of lead-free piezoelectric ceramics. *J. Appl. Phys.* **122,** 014103 (2017).

50. Li, Q., Wei, J., Tu, T., Cheng, J. & Chen, J. Remarkable piezoelectricity and stable high-temperature dielectric properties of quenched $BiFeO_3$-$BaTiO_3$ ceramics. *J. Am. Ceram. Soc.* **100,** 5573–5583 (2017).

51. Wang, T. *et al.* Microstructure and ferroelectric properties of Nb_2O_5-modified $BiFeO_3$-$BaTiO_3$ lead-free ceramics for energy storage. *Mater. Lett.* **137,** 79–81 (2014).

52. Fan, Q. *et al.* Normal-to-relaxor ferroelectric phase transition and electrical properties in Nb-modified $0.72BiFeO_3$-$0.28BaTiO_3$ ceramics. *J. Electroceramics* **36,** 1–7 (2016).

53. Filik, J. *et al.* Processing two-dimensional X-ray diffraction and small-angle scattering data in DAWN 2. *J. Appl. Crystallogr.* **50,** 959–966 (2017).

54. Daniel, L. *et al.* Revisiting the blocking force test on ferroelectric ceramics using high energy x-ray diffraction. *J. Appl. Phys.* **117,** 174104 (2015).

55. Stewart, M., Cain, M. G. & Hall, D. Ferroelectric hysteresis measurement & analysis. *NPL Rep. C. 152* 1–57 (1999).

56. Amirov, A. A. *et al.* Magnetoelectric interactions in $BiFeO_3$, $Bi_{0.95}Nd_{0.05}FeO_3$, and $Bi_{0.95}La_{0.05}FeO_3$ multiferroics. *Tech. Phys. Lett.* **34,** 760–762 (2008).

57. Park, Y. & Kim, Y. H. The Dielectric Temperature Characteristic of Additives Modified Barium-Titanate Having Core-Shell Structured Ceramics. *J. Mater. Res.* **10,** 2770–2776 (1995).

View Article Online
DOI: 10.1039/C7TA09497C

58. Park, Y. & Kim, H. Dielectric temperature characteristics of cerium-modified barium titanate based ceramics with core-shell grain structure. *J. Am. Ceram. Soc.* **80,** 106–112 (1997).

59. Hennings, D. & Rosenstein, G. Temperature-stable dielectrics based on chemically inhomogeneous $BaTiO_3$. *J. Am. Ceram. Soc.* **67,** 249–254 (1984).

60. Armstrong, T. R. & Buchanan, R. C. Influence of core-shell grains on the internal stress state and permittivity response of zirconia-modified barium titanate. *J. Am. Ceram. Soc.* **73,** 1268–1273 (1990).

61. Liu, X., Cheng, S. & Randall, C. The core-shell structure in ultrafine X7R dielectric ceramics. *J. Korean Phys. Soc.* **32,** S312 – S315 (1998).

62. Dean, J. S., Foeller, P. Y., Reaney, I. M. & Sinclair, D. C. A resource efficient design strategy to optimise the temperature coefficient of capacitance of $BaTiO_3$ -based ceramics using finite element modelling. *J. Mater. Chem. A* **4,** 6896–6901 (2016).

63. Yang, H. *et al.* Piezoelectric properties and temperature stabilities of Mn- and Cu-modified $BiFeO_3$-$BaTiO_3$ high temperature ceramics. *J. Eur. Ceram. Soc.* **33,** 1177–1183 (2013).

64. Koruza, J. *et al.* Formation of the core-shell microstructure in lead-free $Bi_{1/2}Na_{1/2}TiO_3$-$SrTiO_3$ piezoceramics and its influence on the electromechanical properties. *J. Eur. Ceram. Soc.* **36,** 1009–1016 (2016).

65. Shannon, R. D. Revised effective ionic radii and systematic studies of interatomic distances in halides and chaleogenides. *Acta Cryst.* **A 32,** 751–767 (1976).

66. Selbach, S. M., Tybell, T., Einarsrud, M. & Grande, T. Size-dependent properties of multiferroic $BiFeO_3$ nanoparticles. *Chem. Mater.* **19,** 6478–6484 (2007).

67. Singh, K., Acharya, S. A. & Bhoga, S. S. Nanosized ceria-based ceramics: A comparative study. *Ionics.* **12,** 295–301 (2006).

68. Zhang, S. T., Lu, M. H., Wu, D., Chen, Y. F. & Ming, N. B. Larger polarization and weak ferromagnetism in quenched $BiFeO_3$ ceramics with a distorted rhombohedral crystal structure. *Appl. Phys. Lett.* **87,** 262907 (2005).

69. Soda, M., Matsuura, M., Wakabayashi, Y. & Hirota, K. Superparamagnetism induced by polar nanoregions in relaxor ferroelectric (1-x)$BiFeO_3$–x$BaTiO_3$. *J. Phys. Soc. Japan* **80,** 043705 (2011).

70. Yoneda, Y., Yoshii, K., Kohara, S., Kitagawa, S. & Mori, S. Local structure of $BiFeO_3$–$BaTiO_3$ mixture. *Jpn. J. Appl. Phys.* **47,** 7590–7594 (2008).

71. Llobet, A., Frontera, C., García-Muñoz, J. L., Ritter, C. & Aranda, M. A. G. Chemical heterogeneity in a single phase: $Bi_{0.15}Ca_{0.85}MnO_3$, a case example of macroscopic phase segregation. *Chem. Mater.* **12,** 3648–3657 (2000).

View Article Online
DOI: 10.1039/C7TA09497C

72. Stephens, P. W. Phenomenological model of anisotropic peak broadening in powder diffraction. *J. Appl. Cryst.* **32,** 281–289 (1999).

73. Dolgos, M. *et al.* Chemical control of octahedral tilting and off-axis A cation displacement allows ferroelectric switching in a bismuth-based perovskite. *Chem. Sci.* **3,** 1426–1435 (2012).

74. Singh, A., Moriyoshi, C., Kuroiwa, Y. & Pandey, D. Evidence for local monoclinic structure, polarization rotation, and morphotropic phase transitions in (1-x)$BiFeO_3$-x$BaTiO_3$ solid solutions: A high-energy synchrotron x-ray powder diffraction study. *Phys. Rev. B* **88,** 024113 (2013).

75. Morozov, M. I., Einarsrud, M.-A. & Grande, T. Atmosphere controlled conductivity and Maxwell-Wagner relaxation in $Bi_{0.5}K_{0.5}TiO_3$-$BiFeO_3$ ceramics. *J. Appl. Phys.* **115,** 044104 (2014).

76. Ogihara, H., Randall, C. A. & Trolier-McKinstry, S. Weakly coupled relaxor behavior of $BaTiO_3$-$BiScO_3$ ceramics. *J. Am. Ceram. Soc.* **92,** 110–118 (2009).

77. Kiyanagi, R. *et al.* Structural and magnetic phase determination of (1-x)$BiFeO_3$-x$BaTiO_3$ solid solution. *J. Phys. Soc. Japan* **81,** 024603 (2012).

78. Wei, Y. *et al.* Polar order evolutions near the rhombohedral to pseudocubic and tetragonal to pseudocubic phase boundaries of the $BiFeO_3$-$BaTiO_3$ system. *Materials.* **8,** 8355–8365 (2015).

79. Yao, Z. *et al.* Greatly reduced leakage current and defect mechanism in atmosphere sintered $BiFeO_3$-$BaTiO_3$ high temperature piezoceramics. *J. Mater. Sci. Mater. Electron.* **25,** 4975–4982 (2014).

80. Cen, Z. *et al.* Structural, ferroelectric and piezoelectric properties of Mn-modified $BiFeO_3$-$BaTiO_3$ high-temperature ceramics. *J. Mater. Sci. Mater. Electron.* **24,** 3952–3957 (2013).

81. Liu, X., Xu, Z., Qu, S., Wei, X. & Chen, J. Ferroelectric and ferromagnetic properties of Mn-doped 0.7$BiFeO_3$-0.3$BaTiO_3$ solid solution. *Ceram. Int.* **34,** 797–801 (2008).

82. Kan, D. *et al.* Universal behavior and electric-field-induced structural transition in rare-earth-substituted $BiFeO_3$. *Adv. Funct. Mater.* **20,** 1108–1115 (2010).

83. Tan, X., Ma, C., Frederick, J., Beckman, S. & Webber, K. G. The antiferroelectric ↔ ferroelectric phase transition in lead-containing and lead-free perovskite ceramics. *J. Am. Ceram. Soc.* **94,** 4091–4107 (2011).

84. Yuan, G. L., Yang, Y. & Or, S. W. Aging-induced double ferroelectric hysteresis loops in $BiFeO_3$ multiferroic ceramic. *Appl. Phys. Lett.* **91,** 122907 (2007).

85. Lo, V., Chung, W. W., Cao, H. & Dai, X. Investigating the effect of oxygen vacancy on the dielectric and electromechanical properties in ferroelectric ceramics. *J. Appl. Phys.* **104,** 064105 (2008).

View Article Online
DOI: 10.1039/C7TA09497C

86. Jo, W. *et al.* Giant electric-field-induced strains in lead-free ceramics for actuator applications - Status and perspective. *J. Electroceramics* **29,** 71–93 (2012).

87. Rojac, T., Kosec, M., Budic, B., Setter, N. & Damjanovic, D. Strong ferroelectric domain-wall pinning in $BiFeO_3$ ceramics. *J. Appl. Phys.* **108,** 074107 (2010).

88. Ke, S. *et al.* Tuning of dielectric and ferroelectric properties in single phase $BiFeO_3$ ceramics with controlled Fe^{2+}/ Fe^{3+} ratio. *Ceram. Int.* **40,** 5263–5268 (2014).

89. Walker, J. *et al.* Synthesis-phase-composition relationship and high electric-field-induced electromechanical behavior of samarium-modified $BiFeO_3$ ceramics. *Acta Mater.* **83,** 149–159 (2015).

90. Cheng, C.-J., Kan, D., Anbusathaiah, V., Takeuchi, I. & Nagarajan, V. Microstructure-electromechanical property correlations in rare-earth-substituted $BiFeO_3$ epitaxial thin films at morphotropic phase boundaries. *Appl. Phys. Lett.* **97,** 212905 (2010).

91. Cheng, C.-J. *et al.* Structural transitions and complex domain structures across a ferroelectric-to-antiferroelectric phase boundary in epitaxial Sm-doped $BiFeO_3$ thin films. *Phys. Rev. B* **80,** 014109 (2009).

92. Acosta, M. *et al.* Core-shell lead-free piezoelectric ceramics: Current status and advanced characterization of the $Bi_{1/2}Na_{1/2}TiO_3$-$SrTiO_3$ system. *J. Am. Ceram. Soc.* **98,** 3405–3422 (2015).

93. Liu, N. *et al.* Revealing the core-shell interactions of a giant strain relaxor ferroelectric $0.75Bi_{1/2}Na_{1/2}TiO_3$-$0.25SrTiO_3$. *Sci. Rep.* **6,** 36910 (2016).

94. Lv, J., Lou, X. & Wu, J. Defect dipole-induced poling characteristics and ferroelectricity of quenched bismuth ferrite-based ceramics. *J. Mater. Chem. C* **4,** 6140–6151 (2016).

95. Yang, H., Yan, F., Lin, Y., Wang, T. & Wang, F. High energy storage density over a broad temperature range in sodium bismuth titanate-based lead-free ceramics. *Sci. Rep.* **7,** 8726 (2017).

96. Yang, H. *et al.* A lead free relaxation and high energy storage efficiency ceramics for energy storage applications. *J. Alloys Compd.* **710,** 436–445 (2017).

97. Shen, Z., Wang, X., Luo, B. & Li, L. $BaTiO_3$–$BiYbO_3$ perovskite materials for energy storage applications. *J. Mater. Chem. A* **3,** 18146–18153 (2015).

98. Yang, Z. *et al.* Significantly enhanced recoverable energy storage density in potassium–sodium niobate-based lead free ceramics. *J. Mater. Chem. A* **4,** 13778–13785 (2016).

99. Mishra, A., Majumdar, B. & Ranjan, R. A complex lead-free (Na, Bi, Ba)(Ti, Fe)O_3 single phase perovskite ceramic with a high energy-density and high discharge-efficiency for solid state capacitor applications. *J. Eur. Ceram. Soc.* **37,** 2379–2384 (2017).

View Article Online
DOI: 10.1039/C7TA09497C

100. Tunkasiri, T. & Rujijanagul, G. Dielectric strength of fine grained barium titanate ceramics. *J. Mater. Sci. Lett.* **15,** 1767–1769 (1996).

101. Liu, B., Wang, X., Zhang, R. & Li, L. Grain size effect and microstructure influence on the energy storage properties of fine-grained $BaTiO_3$-based ceramics. *J. Am. Ceram. Soc.* **100,** 3599–3607 (2017).

102. Wu, L. *et al.* Core-satellite $BaTiO_3$@$SrTiO_3$ assemblies for a local compositionally graded relaxor ferroelectric capacitor with enhanced energy storage density and high energy efficiency. *J. Mater. Chem. C* **3,** 750–758 (2015).

103. Wu, L., Wang, X. & Li, L. Core-shell $BaTiO_3$@$BiScO_3$particles for local graded dielectric ceramics with enhanced temperature stability and energy storage capability. *J. Alloys Compd.* **688,** 113–121 (2016).

104. Wu, L., Wang, X. & Li, L. Enhanced Energy Density in Core-Shell Ferroelectric Ceramics: Modeling and Practical Conclusions. *J. Am. Ceram. Soc.* **99,** 930–937 (2016).

105. He, D., Wang, Y., Chen, X. & Deng, Y. Core-shell structured $BaTiO_3$@Al_2O_3 nanoparticles in polymer composites for dielectric loss suppression and breakdown strength enhancement. *Compos. Part A Appl. Sci. Manuf.* **93,** 137–143 (2017).

106. Hall, D. A., Steuwer, A., Cherdhirunkorn, B., Mori, T. & Withers, P. J. A high energy synchrotron x-ray study of crystallographic texture and lattice strain in soft lead zirconate titanate ceramics. *J. Appl. Phys.* **96,** 4245–4252 (2004).

107. Daniels, J. E., Finlayson, T. R., Studer, A. J., Hoffman, M. & Jones, J. L. Time-resolved diffraction measurements of electric-field-induced strain in tetragonal lead zirconate titanate. *J. Appl. Phys.* **101,** 094104 (2007).

108. Kim, S. *et al.* Structural and electrical characteristics of potential candidate lead-free $BiFeO_3$-$BaTiO_3$ piezoelectric ceramics. *J. Appl. Phys.* **122,** 164105 (2017).

109. Khomchenko, V. A., Karpinsky, D. V. & Paixão, J. A. Magnetostructural correlations in $BiFeO_3$-based multiferroics. *J. Mater. Chem. C* **5,** 3623–3629 (2017).

110. Lv, J., Zhao, H., Wu, M., Lou, X. & Wu, J. Modulating the electric and magnetic properties of $BiFeO_3$ ceramics. *Mater. Des.* **125,** 213–221 (2017).

111. Lennox, R. C. *et al.* Strain driven structural phase transformations in dysprosium doped $BiFeO_3$ ceramics. *J. Mater. Chem. C* **2,** 3345–3360 (2014).

112. Paudel, T. R., Jaswal, S. S. & Tsymbal, E. Y. Intrinsic defects in multiferroic $BiFeO_3$ and their effect on magnetism. *Phys. Rev. B* **85,** 104409 (2012).

113. Tamilselvan, A. *et al.* Role of oxygen vacancy and Fe–O–Fe bond angle in compositional, magnetic, and dielectric relaxation on Eu-substituted $BiFeO_3$ nanoparticles. *Dalt. Trans.* **43,** 5731–5738 (2014).

View Article Online
DOI: 10.1039/C7TA09497C

114. Nan, C.-W., Bichurin, M. I., Dong, S., Viehland, D. & Srinivasan, G. Multiferroic magnetoelectric composites: Historical perspective, status, and future directions. *J. Appl. Phys.* **103,** 031101 (2008).

115. Kumar, A. S. *et al.* Multiferroic and magnetoelectric properties of $Ba_{0.85}Ca_{0.15}Zr_{0.1}Ti_{0.9}O_3$-$CoFe_2O_4$ core-shell nanocomposite. *J. Magn. Magn. Mater.* **418,** 294–299 (2015).

116. Huang, Z. J., Cao, Y., Sun, Y. Y., Xue, Y. Y. & Chu, C. W. Coupling between the ferroelectric and antiferromagnetic orders in $YMnO_3$. *Phys. Rev. B* **56,** 2623–2626 (1997).

117. Kimura, T. *et al.* Magnetocapacitance effect in multiferroic in $BiMnO_3$. *Phys. Rev. B* **67,** 180401 (2003).

118. Kumari, S. *et al.* Dielectric anomalies due to grain boundary conduction in chemically substituted $BiFeO_3$. *J. Appl. Phys.* **117,** 114102 (2015).

View Article Online
DOI: 10.1039/C7TA09497C

Table of Content Entry

The structure and key functional properties of a promising lead-free solid solution, $BiFeO_3$-$BaTiO_3$, have been optimised by controlling chemical homogeneity via La-substitution strategies and thermal treatment.

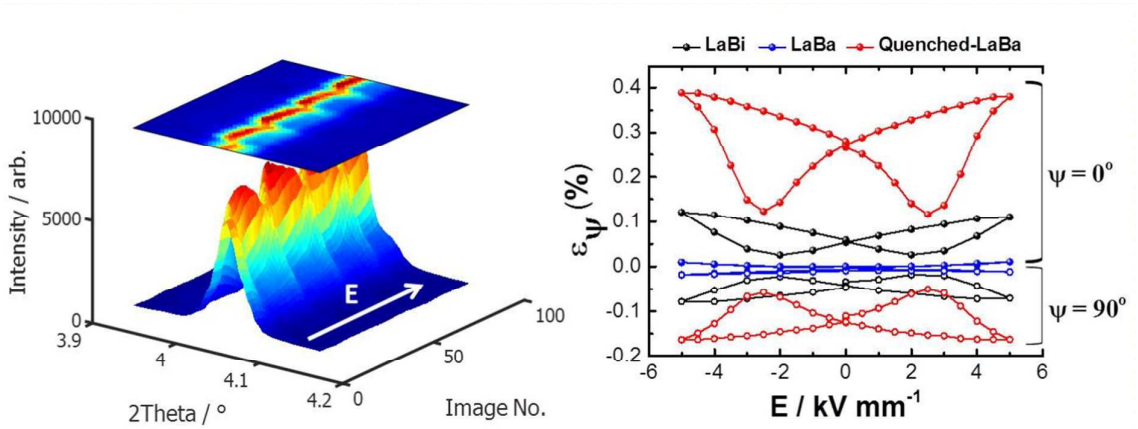

Electronic Supplementary Material (ESI) for Journal of Materials Chemistry A.

Supplementary Information

Optimisation of functional properties in lead-free $BiFeO_3$-$BaTiO_3$ ceramics through La^{3+} substitution strategy

Ilkan Calisir,[1] Abdulkarim. A. Amirov,[2,3] Annette K. Kleppe[4] and David A. Hall[1*]

[1]School of Materials, University of Manchester, M13 9PL, Manchester, UK

[2]Center for Functionalized Magnetic Materials (FunMagMa) & Institute of Physics Mathematics and Informational Technologies Immanuel Kant Baltic Federal University, Kaliningrad, Russia

[3]Amirkhanov Institute of Physics Daghestan Scientific Center, Russian Academy of Sciences Makhachkala, Russia

[4]Diamond Light Source Ltd., Harwell Science and Innovation Campus, OX11 0DE, Didcot, UK

[*]Corresponding Author: david.a.hall@manchester.ac.uk

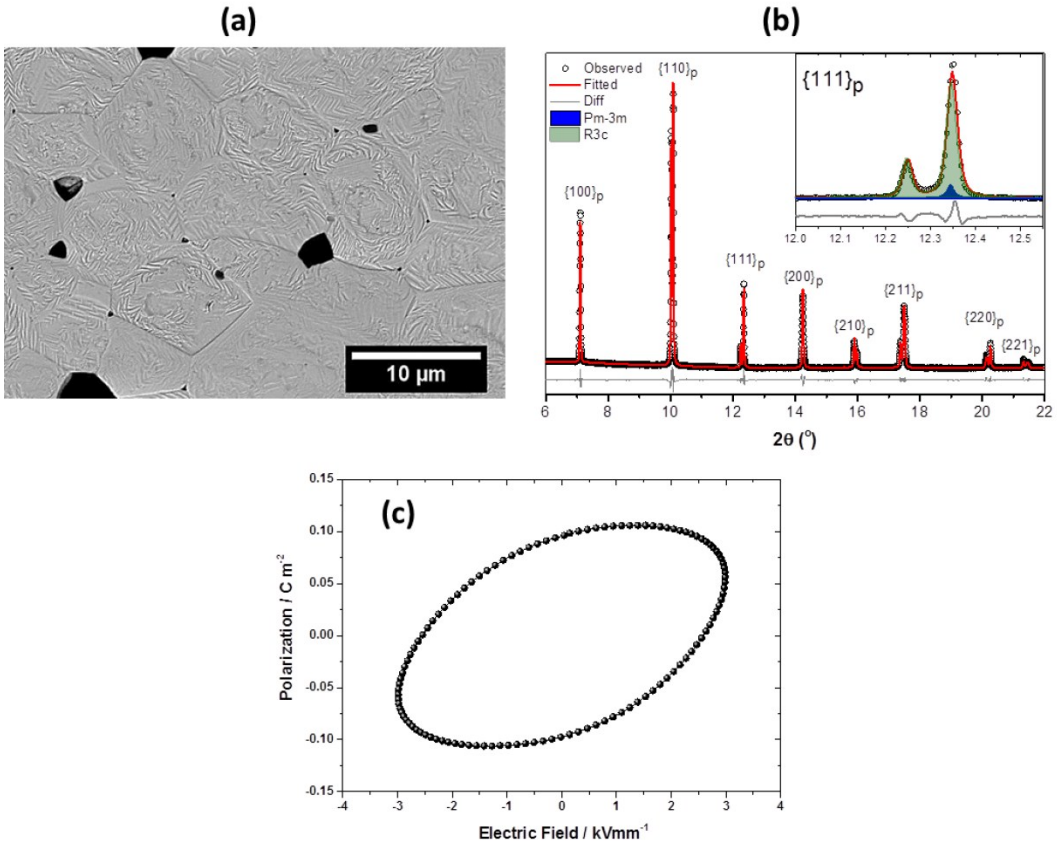

Figure S1. (a) Microstructure, **(b)** refined XRD pattern and **(c)** ferroelectric P-E hysteresis loop of undoped 75BFBT ceramics.

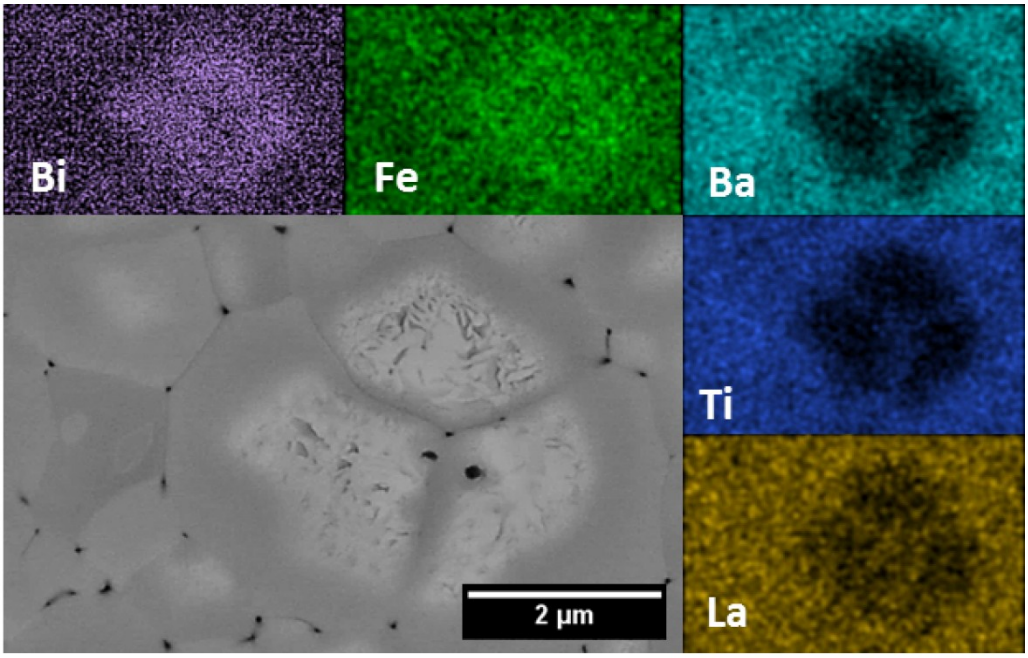

Figure S2. SEM-EDS elemental mapping results for 3 mol% La^{3+} substitution for Ba^{2+} in 75BFBT. The polished surface was chemically etched to reveal its distinct core-shell feature.

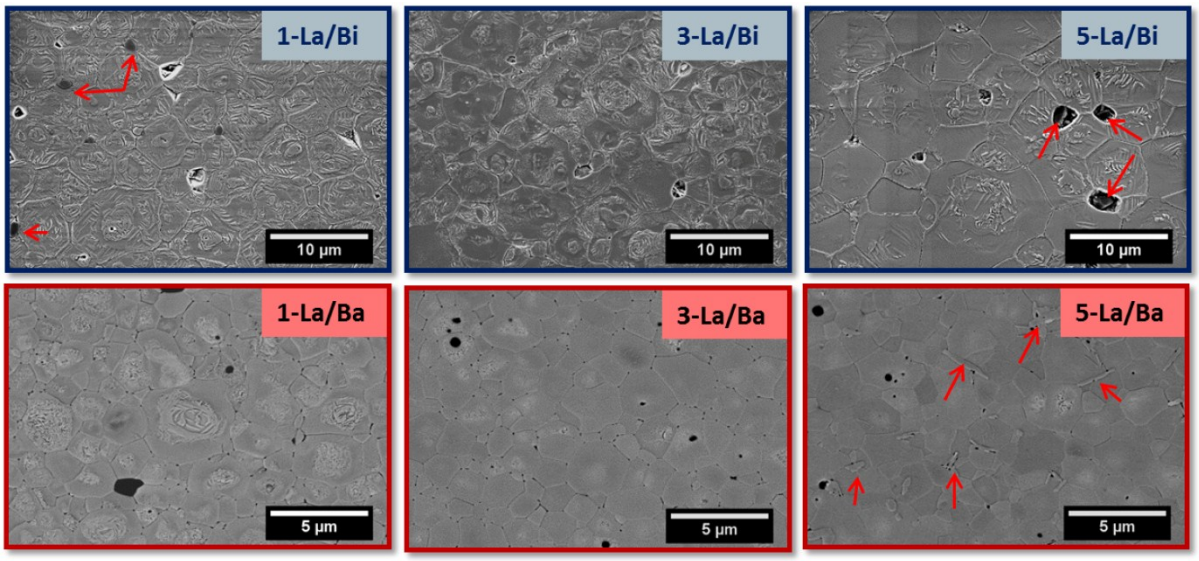

Figure S3. Microstructure of 75BFBT ceramics with 1, 3 and 5 mol% La^{3+} substitution for Bi^{3+} (upper row, denoted as *x*-La/Bi) and for Ba^{2+} (bottom row, denoted as *x*-La/Ba). The polished surfaces were chemically etched. The arrows indicate detected secondary phases.

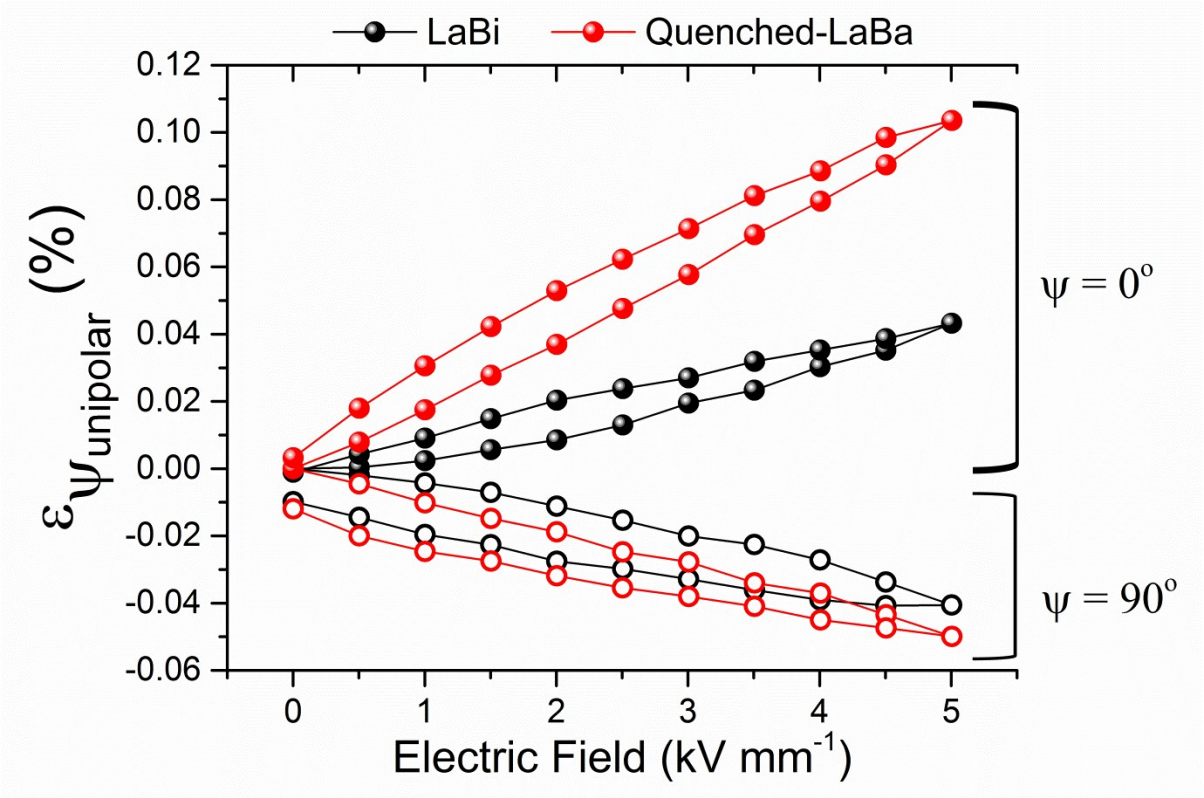

Figure S4. Unipolar macroscopic strain curves of LaBi and quenched-LaBa compositions at Ψ=0˚ and Ψ=90˚

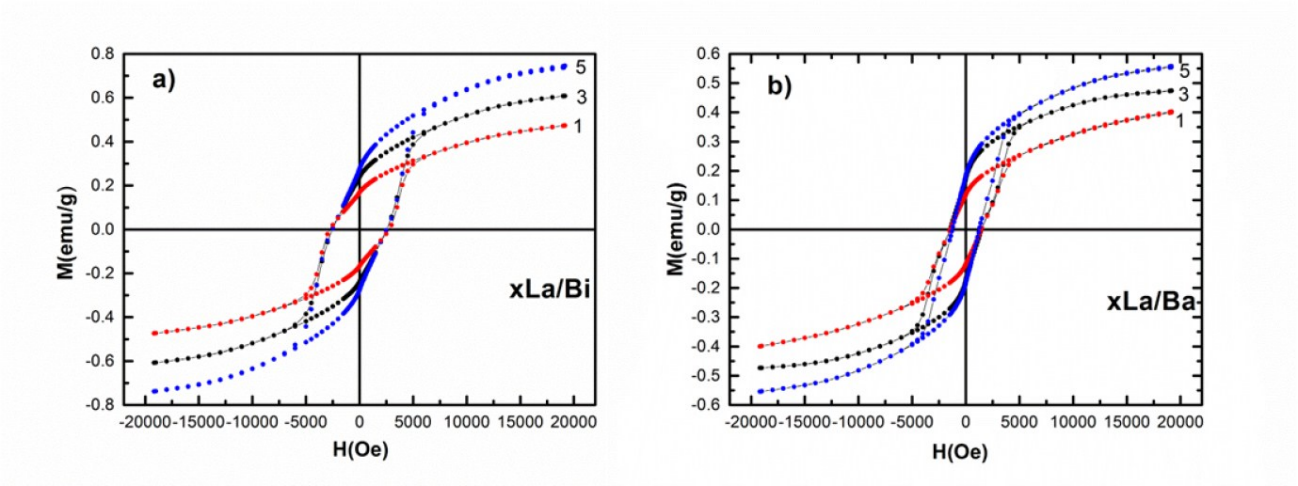

Figure S5. Ferromagnetic (M-H) hysteresis loops of 75BFBT ceramics with **(a)** 1, 3 and 5 mol% La^{3+} substitution for Bi^{3+} (denoted as *x*La/Bi), and **(b)** 1, 3 and 5 mol% La^{3+} substitution for Ba^{2+} (denoted as *x*La/Ba).